A stable imaging functional for anisotropic periodic media in electromagnetic inverse scattering

Dinh-Liem Nguyen* Trung Truong†

Abstract

This paper addresses the inverse scattering problem for Maxwell's equations in three dimensional anisotropic periodic media. We study a new imaging functional for the fast and robust reconstruction of the shape of anisotropic periodic scatterers from boundary measurements of the scattered field. The implementation of this imaging functional is simple and avoids the need to solve an ill-posed problem. The resolution and stability analysis of the imaging functional is investigated. Results from our numerical study indicate that this imaging functional is more stable than that of the factorization method and more accurate than that of the orthogonality sampling method in reconstructing periodic scatterers.

Keywords. electromagnetic inverse scattering, periodic media, sampling method, shape reconstruction, photonic crystals

AMS subject classification. 35R30, 78A46, 65C20

1 Introduction

We consider three dimensional periodic media that are unboundedly periodic in say x_1- and x_2-directions and bounded in x_3-direction. These periodic media can model two-dimensional photonic crystals that are popular in optics [8]. We are interested in the inverse problem of determining the shape of these periodic media from boundary measurements of the scattered electromagnetic fields generated by a number of incident fields. This inverse problem comes from the noninvasive imaging of photonic crystals using electromagnetic waves. Noninvasive imaging of photonic crystals is the process of visualizing and characterizing the structure and/or optical properties of photonic crystals without damaging the crystals themselves. This imaging technique is very important for understanding the properties and performance of photonic crystals and is often used in manufacturing to ensure the quality of photonic crystals.

In the past two decades, there has been a substantial body of work on numerical methods for shape reconstruction of periodic media in inverse scattering. Results for Helmholtz-type equations can be found in [1, 2, 6, 7, 9, 10, 12, 13, 18, 20, 23, 24, 27–29], among other references. However, the number of results on numerical reconstructions for the inverse problem associated with full Maxwell's equations in three dimensions has been limited, as seen in [4, 16, 19, 22, 26]. This limitation is evidently due to the technical complexity and high computational demands of Maxwell's equations

*Department of Mathematics, Kansas State University, Manhattan, KS 66506, USA; (dlnguyen@ksu.edu)

†Department of Mathematics & Physics, Marshall University, Huntington, WV 25755, USA; (truongt@marshall.edu)

in three-dimensional periodic media. The methods primarily studied for the case of Maxwell's equations include the factorization method [19,22,26] and the near-field imaging method relying on a transformed field expansion [4,5,16]. The latter method can offer subwavelength resolution, but it requires the periodic scattering layer to be a smooth periodic function multiplied by a small surface deformation parameter. While the factorization method is more flexible concerning the shape and properties (e.g., anisotropic or chiral) of periodic media, it unfortunately lacks robustness against noise in the data.

In this paper, we investigate a novel imaging functional for the reconstruction of anisotropic periodic scatterers for Maxwell's equations in three dimensions. This new imaging functional is not only highly robust against noise in the data but also flexible when it comes to different shapes of periodic scattering media. The implementation of the imaging functional is straightforward, computationally efficient, and rapid since it involves evaluating a double sum, essentially encompassing a finite number of propagating modes in the scattered field data. Moreover, the implementation does not require solving any ill-posed problems. We prove that the imaging functional is associated with a volume integral over the periodic scatterer in one unit cell, and this volume integral has a kernel that strongly peaks when the sampling point is inside the periodic scatterer. The stability of the imaging functional is also rigorously justified. The numerical study further reveals that the proposed sampling method is more stable than the factorization method and more accurate than the orthogonality sampling method in reconstructing periodic scattering media. This work can be considered an extension of the results presented in [23], where the Helmholtz equation case was investigated. Due to the technical complications arising from Maxwell's equations in periodic media, this extension is nontrivial. The imaging functional for the Maxwell case is an infinite series, unlike the finite sum in the scalar case. The extension demands a careful and detailed analysis of a modal version of Green formulas for the quasiperiodic Green's tensor of the direct problem and the quasiperiodic scattered electric field via its volume integro-differential formulation. It is also worth noting that while the orthogonality sampling method has been studied for inverse scattering from bounded objects [11,14,15,17,25], its application to the inverse scattering problem for periodic media is still unknown.

The rest of the paper is organized as follows. We formulate the inverse problem of interest in Section 2. The new imaging functional and its resolution and stability analysis are discussed in Section 3. A numerical study of the new imaging functional is presented in Section 4. Finally, a conclusion summarizing the results we have obtained and some related future research is given in Section 5.

2 Electromagnetic scattering from periodic media

We consider an anisotropic periodic medium in $\mathbb{R}^3$ that is unboundedly 2π-periodic in x_1- and x_2-directions and bounded in x_3-direction. Let $k > 0$ be the wave number and ε be a 3×3 bounded matrix-valued function which represents the permittivity of the medium. We assume that ε is 2π-periodic in the x_1- and x_2-directions, and that in each period $(m_1\pi, (m_1+2)\pi) \times (m_2\pi, (m_2+2)\pi) \times \mathbb{R}$ for any $m_1, m_2 \in \mathbb{Z}$, it is equal to the identity matrix I_3 outside a compact set. This periodic medium is illuminated by an incident electric field $\mathbf{E}^{in} : \mathbb{R}^3 \to \mathbb{C}^3$, which is generated by source function $\mathbf{J} : \mathbb{R}^3 \to \mathbb{C}^3$. Their interaction gives rise to a scattered electric field $\mathbf{u}$ that is also a function from $\mathbb{R}^3$ to $\mathbb{C}^3$. The total field $\mathbf{E} = \mathbf{E}^{in} + \mathbf{u}$ is assumed to satisfy the Maxwell's equations

$$\operatorname{curl}\operatorname{curl}\mathbf{E} - k^2\varepsilon(\mathbf{x})\mathbf{E} = \mathbf{J}, \quad \mathbf{x} \in \mathbb{R}^3. \tag{1}$$

Now for $\alpha = (\alpha_1, \alpha_2) \in \mathbb{R}^2$, a function $\mathbf{f} : \mathbb{R}^3 \to \mathbb{C}^3$ is called α-quasiperiodic if

$$\mathbf{f}(x_1 + m_1 2\pi, x_2 + m_2 2\pi, x_3) = e^{2\pi i(\alpha_1 m_1 + \alpha_2 m_2)} \mathbf{f}(x_1, x_2, x_3) \quad \text{for all } m_1, m_2 \in \mathbb{Z}.$$

Fixing $\alpha = (\alpha_1, \alpha_2)$, we use N α-quasiperiodic incident electric fields to illuminate the periodic medium. Denote these incident fields by $\mathbf{E}^{in}(\cdot, l)$ for $l = 1, \dots N$. More specifically, $\mathbf{E}^{in}(\cdot, l)$ satisfy

$$\operatorname{curl}\operatorname{curl} \mathbf{E}^{in}(\cdot, l) - k^2 \mathbf{E}^{in}(\cdot, l) = \mathbf{J}(\cdot, l), \quad l = 1, \dots N.$$

Following the usual approach we look for α-quasiperiodic scattered fields $\mathbf{u}(\cdot, l)$. We can rewrite (1) for $\mathbf{u}(\cdot, l)$ as follows

$$\operatorname{curl}\operatorname{curl} \mathbf{u}(\cdot, l) - k^2 \mathbf{u}(\cdot, l) = k^2(\varepsilon(\mathbf{x}) - I_3)(\mathbf{u}(\cdot, l) + \mathbf{E}^{in}(\cdot, l)). \tag{2}$$

We complete the scattering problem with the Rayleigh radiation condition. To this end we first introduce some notations. Let $h > 0$ be such that

$$h > \sup\{|x_3| : \mathbf{x} = (x_1, x_2, x_3)^\top \in \operatorname{supp}(\varepsilon - I_3)\}$$

and let

$$\Omega := (-\pi, \pi)^2 \times \mathbb{R}, \quad \Omega_h := (-\pi, \pi)^2 \times (-h, h), \quad \Gamma_{\pm h} := (-\pi, \pi)^2 \times \{\pm h\}.$$

In addition to (2), the scattered electric fields $\mathbf{u}(\cdot, l)$ satisfy the Rayleigh radiation condition, i.e.,

$$\mathbf{u}(\mathbf{x}, l) = \begin{cases} \sum_{j \in \mathbb{Z}^2} \mathbf{u}_j^+(l) e^{i(\alpha_{1,j} x_1 + \alpha_{2,j} x_2 + \beta_j (x_3 - h)} & \text{if } x_3 > h, \\ \sum_{j \in \mathbb{Z}^2} \mathbf{u}_j^-(l) e^{i(\alpha_{1,j} x_1 + \alpha_{2,j} x_2 - \beta_j (x_3 + h)} & \text{if } x_3 < -h, \end{cases} \tag{3}$$

where

$$\alpha_{1,j} = \alpha_1 + j_1, \quad \alpha_{2,j} = \alpha_2 + j_2, \quad \alpha_j = (\alpha_{1,j}, \alpha_{2,j}, 0)^\top$$

and

$$\beta_j = \begin{cases} \sqrt{k^2 - |\alpha_j|^2}, & |\alpha_j| \le k, \\ i\sqrt{|\alpha_j|^2 - k^2}, & |\alpha_j| > k, \end{cases} \tag{4}$$

for all $j = (j_1, j_2) \in \mathbb{Z}^2$. The sequences of coefficients $(\mathbf{u}_j^+(l))_j$ and $(\mathbf{u}_j^-(l))_j$ are called the Rayleigh sequences of $\mathbf{u}(\cdot, l)$ and can be computed by

$$\mathbf{u}_j^\pm(l) = \frac{1}{4\pi^2} \int_{\Gamma_{\pm h}} \mathbf{u}(\mathbf{x}, l) e^{-i(\alpha_{1,j} x_1 + \alpha_{2,j} x_2)} \mathrm{d}s(\mathbf{x}). \tag{5}$$

Note that all but finitely many terms in (3) are exponentially decaying, which helps us easily deduce pointwise absolute convergence of the series. The exponentially decaying terms in (3) are called evanescent modes and the terms corresponding to real β_j's are called propagating modes. Moreover, we need β_j to be nonzero for all $j \in \mathbb{Z}^2$, in other words, k is not a Wood's anomaly. The technical reason behind this assumption is that the representation of the α-quasiperiodic Green's function we use in (6) is not well-defined at a Wood's anomaly. For the study of the inverse problem in this paper, we assume that the direct problem (2)-(3) is well-posed. We refer to [5, 21] for studies on well-posedness of the direct problem (2)-(3).

Note that since the scattering medium is 2π-periodic in x_1 and x_2, finding its geometry in Ω is sufficient. Denote by D the geometry of the medium in Ω, i.e.

$$D := \operatorname{supp}(\varepsilon - I_3) \cap \Omega.$$

We aim to solve the following inverse problem.

Inverse Problem. Given measurement of multiple scattered electric fields $\mathbf{u}(\cdot, l)$ on $\Gamma_{\pm h}$ corresponding to multiple incident fields $\mathbf{E}^{in}(\cdot, l)$, $l = 1, \dots, N$, find D in Ω_h.

3 A new imaging functional

We will introduce a new imaging functional to solve the stated inverse problem and analyze its behavior in this section. To this end, we first need the quasiperiodic Green's tensor of the direct problem. For $\mathbf{x}-\mathbf{y} \neq (2\pi m_1, 2\pi m_2, 0)$, for all $m_1, m_2 \in \mathbb{Z}$, the α-quasiperiodic Green's tensor of the direct problem is given by (see, e.g., [26])

$$\mathbb{G}(\mathbf{x},\mathbf{y}) := \Phi(\mathbf{x},\mathbf{y})I_3 + \frac{1}{k^2}\nabla_{\mathbf{x}}\mathrm{div}_{\mathbf{x}}(\Phi(\mathbf{x},\mathbf{y})I_3),$$

where the divergence is taken columnwise and the gradient is taken componentwise. $\Phi(\mathbf{x},\mathbf{y})$ is the α-quasiperiodic Green's function of the scalar Helmholtz problem,

$$\Phi(\mathbf{x},\mathbf{y}) := \frac{i}{8\pi^2}\sum_{j\in\mathbb{Z}^2}\frac{1}{\beta_j}e^{i(\alpha_{1,j}(x_1-y_1)+\alpha_{2,j}(x_2-y_2)+\beta_j|x_3-y_3|)}, \tag{6}$$

with Rayleigh coefficients given by

$$r_j^{\pm}(\mathbf{y}) = \frac{i}{8\pi^2\beta_j}e^{-i\alpha_{1,j}y_1-i\alpha_{2,j}y_2+i\beta_j(h\mp y_3)}. \tag{7}$$

Lemma 1. *For $\mathbf{z}\in\Omega_h$, the columns of $\mathbb{G}(\cdot,\mathbf{z})$ satisfy the Rayleigh radiation condition (3). Let $G_{mn}(\cdot,\mathbf{z})$ be the entry on the m-th row, n-th column of $\mathbb{G}(\cdot,\mathbf{z})$. Then, the Rayleigh sequences $(g_{mn}^{\pm})_j(\mathbf{z})$ of $G_{mn}(\cdot,\mathbf{z})$ can be given as an expression in terms of $r_j^{\pm}(\mathbf{z})$,*

$$(g_{mn}^{\pm})_j(\mathbf{z}) = \left(\delta_{mn} - \frac{\gamma_{m,j}^{\pm}\gamma_{n,j}^{\pm}}{k^2}\right) r_j^{\pm}(\mathbf{z}), \quad j\in\mathbb{Z}^2,$$

where δ_{mn} is the Kronecker delta and

$$\gamma_{n,j}^{\pm} := \begin{cases} \alpha_{n,j} & \text{if } n=1,2,\\ \pm\beta_j & \text{if } n=3. \end{cases}$$

Proof. For $\mathbf{x}\in\Omega$ with $x_3 > h$ and $\mathbf{z}\in\Omega_h$,

$$\Phi(\mathbf{x},\mathbf{z}) = \sum_{j\in\mathbb{Z}^2} r_j^{+}(\mathbf{z})e^{i(\alpha_{1,j}x_1+\alpha_{2,j}x_2+\beta_j(x_3-h))},$$

thus,

$$\begin{aligned}
\mathbb{G}(\mathbf{x},\mathbf{z}) &= \Phi(\mathbf{x},\mathbf{y})I_3 + \frac{1}{k^2}\nabla_{\mathbf{x}}\mathrm{div}_{\mathbf{x}}(\Phi(\mathbf{x},\mathbf{y})I_3)\\
&= \sum_{j\in\mathbb{Z}^2}\left(\begin{bmatrix}1&0&0\\0&1&0\\0&0&1\end{bmatrix} + \frac{1}{k^2}\begin{bmatrix}\frac{\partial^2}{\partial x_1^2} & \frac{\partial^2}{\partial x_1\partial x_2} & \frac{\partial^2}{\partial x_1\partial x_3}\\ \frac{\partial^2}{\partial x_2\partial x_1} & \frac{\partial^2}{\partial x_2^2} & \frac{\partial^2}{\partial x_2\partial x_3}\\ \frac{\partial^2}{\partial x_3\partial x_1} & \frac{\partial^2}{\partial x_3\partial x_2} & \frac{\partial^2}{\partial x_3^2}\end{bmatrix}\right) r_j^{+}(\mathbf{z})e^{i(\alpha_{1,j}x_1+\alpha_{2,j}x_2+\beta_j(x_3-h))}\\
&= \sum_{j\in\mathbb{Z}^2}\left(\begin{bmatrix}1&0&0\\0&1&0\\0&0&1\end{bmatrix} - \frac{1}{k^2}\begin{bmatrix}\alpha_{1,j}^2 & \alpha_{1,j}\alpha_{2,j} & \alpha_{1,j}\beta_j\\ \alpha_{2,j}\alpha_{1,j} & \alpha_{2,j}^2 & \alpha_{2,j}\beta_j\\ \beta_j\alpha_{1,j} & \beta_j\alpha_{2,j} & \beta_j^2\end{bmatrix}\right) r_j^{+}(\mathbf{z})e^{i(\alpha_{1,j}x_1+\alpha_{2,j}x_2+\beta_j(x_3-h))}\\
&= \sum_{j\in\mathbb{Z}^2}\left[\delta_{mn} - \frac{\gamma_{m,j}^{+}\gamma_{n,j}^{+}}{k^2}\right]_{mn} r_j^{+}(\mathbf{z})e^{i(\alpha_{1,j}x_1+\alpha_{2,j}x_2+\beta_j(x_3-h))}.
\end{aligned}$$

Similarly, we can show that, for $x \in \Omega$ such that $x_3 < -h$,

$$\mathbb{G}(\mathbf{x}, \mathbf{z}) = \sum_{j \in \mathbb{Z}^2} \left[\delta_{mn} - \frac{\gamma_{m,j}^- \gamma_{n,j}^-}{k^2} \right]_{mn} r_j^-(\mathbf{z}) e^{i(\alpha_{1,j} x_1 + \alpha_{2,j} x_2 - \beta_j (x_3 + h))}.$$

This shows that, each entry $G_{mn}(\cdot, \mathbf{z})$ of $\mathbb{G}(\cdot, \mathbf{z})$ admits a Rayleigh series representation for $x_3 > h$ or $x_3 < -h$. Therefore, the columns of $\mathbb{G}(\cdot, \mathbf{z})$ satisfy the Rayleigh radiation condition and the Rayleigh coefficients of $G_{mn}(\cdot, \mathbf{z})$ are given by

$$(g_{mn}^{\pm})_j(\mathbf{z}) = \left(\delta_{mn} - \frac{\gamma_{m,j}^{\pm} \gamma_{n,j}^{\pm}}{k^2} \right) r_j^{\pm}(\mathbf{z}).$$

□

For $j \in \mathbb{Z}^2$, we denote

$$\mathbf{g}_j^{\pm}(\mathbf{z}) := \left[(g_{mn}^{\pm})_j(\mathbf{z}) \right]_{mn}, \quad \mathbf{h}_j^{\pm}(\mathbf{z}) := \begin{bmatrix} \alpha_{1,j}(g_{31}^{\pm})_j & \alpha_{1,j}(g_{32}^{\pm})_j & \alpha_{1,j}(g_{33}^{\pm})_j \\ \alpha_{2,j}(g_{31}^{\pm})_j & \alpha_{2,j}(g_{32}^{\pm})_j & \alpha_{2,j}(g_{33}^{\pm})_j \\ \pm\beta_j(g_{31}^{\pm})_j & \pm\beta_j(g_{32}^{\pm})_j & \pm\beta_j(g_{33}^{\pm})_j \end{bmatrix} (\mathbf{z}).$$

Now with the data $\mathbf{u}(\cdot, l)$ given on $\Gamma_{\pm h}$ for $l = 1, \ldots, N$, we can compute the Rayleigh coefficients $\mathbf{u}_j^{\pm}(l) = \begin{bmatrix} u_{1,j}^{\pm}(l) & u_{2,j}^{\pm}(l) & u_{3,j}^{\pm}(l) \end{bmatrix}^{\top}$ via (5). We define the imaging functional as

$$\mathcal{I}(\mathbf{z}) := \sum_{l=1}^{N} \left| \sum_{j \in \mathbb{Z}^2} \left(\left(\mathbf{h}_j^+(\mathbf{z}) - 2\mathrm{Re}\,(\beta_j)\ \mathbf{g}_j^+(\mathbf{z}) \right)^* \mathbf{u}_j^+(l) + u_{3,j}^+(l) \mathbf{g}_j^+(\mathbf{z})^* \begin{bmatrix} \alpha_{1,j} \\ \alpha_{2,j} \\ \beta_j \end{bmatrix} \right. \right.$$
$$\left. \left. - \left(\mathbf{h}_j^-(\mathbf{z}) + 2\mathrm{Re}\,(\beta_j)\ \mathbf{g}_j^-(\mathbf{z}) \right)^* \mathbf{u}_j^-(l) - u_{3,j}^-(l) \mathbf{g}_j^-(\mathbf{z})^* \begin{bmatrix} \alpha_{1,j} \\ \alpha_{2,j} \\ -\beta_j \end{bmatrix} \right) \right|^p,$$

where $\mathbf{A}^*$ denotes the transpose conjugate of the matrix $\mathbf{A}$. Here $p > 0$ is chosen to sharpen the reconstruction of the imaging functional (e.g., $p = 3$ works well in the numerical simulations).

Remark 2. *We note that the Rayleigh sequences $(r_j^{\pm}(\mathbf{z}))_j$ in (7) are exponentially decaying as $|j|$ increases and β_j is complex-valued. For $m, n = 1, 2, 3$, the sequences $((g_{mn}^{\pm})_j(\mathbf{z}))_j$ involve $r_j^{\pm}(\mathbf{z})$ multiplied by β_j and $\alpha_{1,j}$ or $\alpha_{2,j}$. Thus these sequences are quickly decaying as $|j|$ increases and β_j is complex-valued. This property holds for all $\mathbf{z} \in \Omega_h$. This leads to the fact that $\mathbf{g}_j^{\pm}(\mathbf{z})$ and $\mathbf{h}_j^{\pm}(\mathbf{z})$ also have quickly decaying entries for complex-valued β_j's. Therefore, $\mathcal{I}(\mathbf{z})$ is well-defined and that only a finite number of terms corresponding to real-valued β_j's may make significant contributions to $\mathcal{I}(\mathbf{z})$ and the terms corresponding to complex-valued β_j's can be essentially ignored. This is confirmed in the numerical study.*

Define the Sobolev spaces $H_\alpha(\mathrm{curl}\,, \Omega_h)$ and $H_{\alpha,\mathrm{loc}}(\mathrm{curl}\,, \Omega)$ as

$$H_\alpha(\mathrm{curl}\,, \Omega_h) := \left\{ \mathbf{w} \in [L^2(\Omega_h)]^3 : \mathrm{curl}\,\mathbf{w} \in [L^2(\Omega_h)]^3 \text{ and } \mathbf{w} = \mathbf{W}|_{\Omega_h} \right.$$
$$\left. \text{for some } \alpha\text{-quasiperiodic } \mathbf{W} \in [L^2_{\mathrm{loc}}(\mathbb{R}^2)]^3 \right\},$$
$$H_{\alpha,\mathrm{loc}}(\mathrm{curl}\,, \Omega) := \left\{ \mathbf{w} \in [L^2_{\mathrm{loc}}(\Omega)]^3 : \mathrm{curl}\,\mathbf{w} \in [L^2_{\mathrm{loc}}(\Omega)]^3 \text{ and } \mathbf{w} = \mathbf{W}|_{\Omega} \right.$$
$$\left. \text{for some } \alpha\text{-quasiperiodic } \mathbf{W} \in [L^2_{\mathrm{loc}}(\mathbb{R}^2)]^3 \right\}.$$

The unique weak solution $\mathbf{u} \in H_{\alpha,\mathrm{loc}}(\mathrm{curl}\,,\Omega)$ of the direct problem (2)-(3) satisfies the Rayleigh radiation condition (3) and

$$\int_\Omega \mathrm{curl}\,\mathbf{u}(\mathbf{x}) \cdot \mathrm{curl}\,\overline{\mathbf{v}(\mathbf{x})} - k^2 \mathbf{u}(\mathbf{x}) \cdot \overline{\mathbf{v}(\mathbf{x})}\,\mathrm{d}\mathbf{x} = k^2 \int_D (\varepsilon(\mathbf{x}) - I_3)(\mathbf{u}(\mathbf{x}) + \mathbf{E}^{in}(\mathbf{x})) \cdot \overline{\mathbf{v}(\mathbf{x})}\,\mathrm{d}\mathbf{x}, \quad (8)$$

for all $\mathbf{v} \in H_\alpha(\mathrm{curl}\,,\Omega_h)$ with compact support. It is known that $\mathbf{u}$ also satisfies the volume integro-differential equation (see, e.g., [21])

$$\mathbf{u}(\mathbf{x}) = (k^2 + \nabla_{\mathbf{x}} \mathrm{div}_{\mathbf{x}}) \int_D \Phi(\mathbf{x},\mathbf{y})(\varepsilon(\mathbf{y}) - I_3)\mathbf{E}(\mathbf{y})\,\mathrm{d}\mathbf{y}. \quad (9)$$

The equivalence is understood in the sense that, if $\mathbf{u} \in H_{\alpha,\mathrm{loc}}(\mathrm{curl}\,,\Omega)$ satisfies (3) and (8) then $\mathbf{u}|_{\Omega_h}$ belongs to $H_\alpha(\mathrm{curl}\,,\Omega_h)$ and solves (9), and conversely, if $\mathbf{u}|_{\Omega_h} \in H_\alpha(\mathrm{curl}\,,\Omega_h)$ solves (9) then it can be extended into a solution of (8) in $H_{\alpha,\mathrm{loc}}(\mathrm{curl}\,,\Omega)$ that also satisfies the radiation condition (3).

We justify the resolution of the imaging functional in the following theorem.

Theorem 3. *The imaging functional $\mathcal{I}(\mathbf{z})$ satisfies*

$$\mathcal{I}(\mathbf{z}) = \sum_{l=1}^{N} \left| \frac{k^2}{2\pi^2} \int_D \mathbb{F}(\mathbf{z},\mathbf{y})\,(\varepsilon(\mathbf{y}) - I_3)\mathbf{E}(\mathbf{y},l)\,\mathrm{d}\mathbf{y} \right|^p, \quad \mathbf{z} \in \Omega_h,$$

where

$$\mathbb{F}(\mathbf{x},\mathbf{y}) = F(\mathbf{x},\mathbf{y})I_3 + \frac{1}{k^2}\nabla_{\mathbf{x}}\mathrm{div}_{\mathbf{x}}(F(\mathbf{x},\mathbf{y})I_3),$$

with

$$F(\mathbf{x},\mathbf{y}) = \frac{k}{4\pi} j_0(k|\mathbf{x}-\mathbf{y}|) + \sum_{(0,0)\neq j\in\mathbb{Z}^2} \frac{k e^{-i2\pi\alpha\cdot j}}{4\pi} j_0\left(k\left|\mathbf{x}-\mathbf{y}+(2\pi j_1, 2\pi j_2, 0)^\top\right|\right)$$

(j_0 is the spherical Bessel function of the first kind of order 0).

Remark 4. *For a fixed $\mathbf{y}$, we numerically observe that the series in $F(\mathbf{x},\mathbf{y})$ makes a relatively small perturbation to $\frac{k}{4\pi} j_0(k|\mathbf{x}-\mathbf{y}|)$ that strongly peaks as $\mathbf{x}$ is close to $\mathbf{y}$ and has much smaller values otherwise. Thus, the behavior of $|F(\mathbf{x},\mathbf{y})|$ is pretty similar to that of $\frac{k}{4\pi} j_0(k|\mathbf{x}-\mathbf{y}|)$ as it can be seen in Figure 1. A two-dimensional version of $F(\mathbf{x},\mathbf{y})$ was studied in [23] with similar behaviors. We can thus expect $\mathbb{F}(\mathbf{x},\mathbf{y})$ to have a similar behavior. Figure 2 shows the values of $|\mathbb{F}(\mathbf{x},0)\mathbf{q}|_2$ when $k = 2\pi$, $\alpha_1 = \alpha_2 = 0$ and for $\mathbf{q} = (0,0,1)^\top$ and $\mathbf{q} = (1,1,1)^\top$. In both cases, $|\mathbb{F}(\mathbf{x},0)\mathbf{q}|_2$ behaves as expected. We also note that similar behaviors of $|\mathbb{F}(\mathbf{x},0)\mathbf{q}|_2$ were observed for $\mathbf{q} = (1,0,0)^\top$ and $\mathbf{q} = (0,1,0)^\top$. Therefore, we expect from Theorem 3 that the imaging functional $\mathcal{I}(\mathbf{z})$ takes larger values as $\mathbf{z}$ is inside D and that $\mathcal{I}(\mathbf{z})$ is much smaller for $\mathbf{z}$ is outside D. This is indeed confirmed in the numerical study.*

Proof. Let $\mathbf{G}_n$ be the n-th column of $\mathbb{G}$, $n = 1,2,3$. For all $\mathbf{x}_s, \mathbf{x}_t \in \Omega_h$ and $\mathbf{x} \in \overline{\Omega_h}$, we have

$$\mathrm{curl}\,\mathrm{curl}\,\mathbf{G}_n(\mathbf{x},\mathbf{x}_s) - k^2\mathbf{G}_n(\mathbf{x},\mathbf{x}_s) = \delta(\mathbf{x}-\mathbf{x}_s)\mathbf{e}_n,$$

and dot-multiplying both sides by $\overline{\mathbf{G}_m(\mathbf{x},\mathbf{x}_t)}$, $m = 1,2,3$ gives

$$\mathrm{curl}\,\mathrm{curl}\,\mathbf{G}_n(\mathbf{x},\mathbf{x}_s) \cdot \overline{\mathbf{G}_m(\mathbf{x},\mathbf{x}_t)} - k^2\mathbf{G}_n(\mathbf{x},\mathbf{x}_s) \cdot \overline{\mathbf{G}_m(\mathbf{x},\mathbf{x}_t)} = \delta(\mathbf{x}-\mathbf{x}_s)\mathbf{e}_n \cdot \overline{\mathbf{G}_m(\mathbf{x},\mathbf{x}_t)}.$$

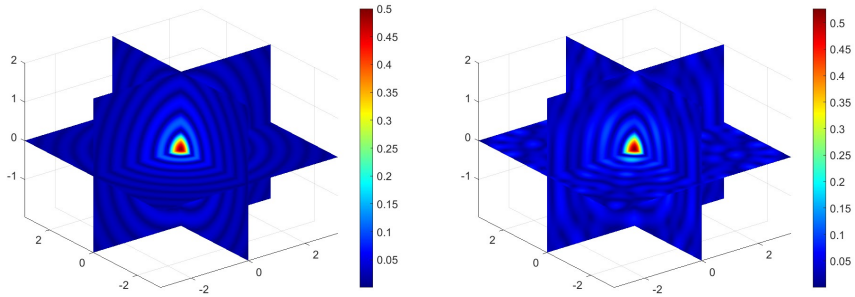

(a) $|\frac{k}{4\pi} j_0(k|\mathbf{x}|)|$ (b) $|F(\mathbf{x},0)|$

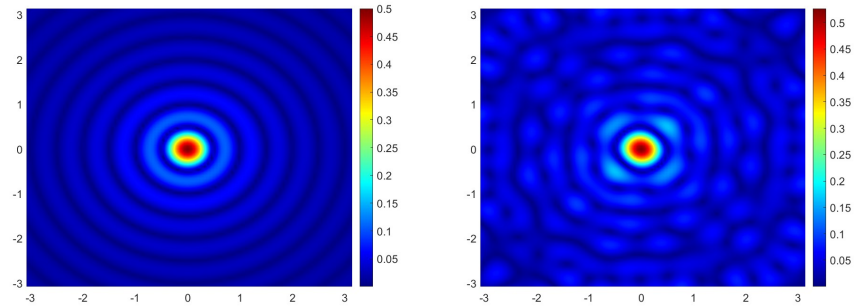

(c) Top view of (a) (d) Top view of (b)

Figure 1: $\left|\frac{k}{4\pi} j_0(k|\mathbf{x}|)\right|$ and $|F(\mathbf{x},0)|$, $k = 2\pi$, $\alpha_1 = \alpha_2 = 0$.

Integrating by part over Ω_h with respect to $\mathbf{x}$ we obtain

$$\int_{\Omega_h} \operatorname{curl} \mathbf{G}_n(\mathbf{x},\mathbf{x}_s) \cdot \operatorname{curl} \overline{\mathbf{G}_m(\mathbf{x},\mathbf{x}_t)}\, \mathrm{d}\mathbf{x} - k^2 \int_{\Omega_h} \mathbf{G}_n(\mathbf{x},\mathbf{x}_s) \cdot \overline{\mathbf{G}_m(\mathbf{x},\mathbf{x}_t)}\, \mathrm{d}\mathbf{x} + \int_{\partial\Omega_h} \nu(\mathbf{x}) \times \operatorname{curl} \mathbf{G}_n(\mathbf{x},\mathbf{x}_s) \cdot \overline{\mathbf{G}_m(\mathbf{x},\mathbf{x}_t)}\, \mathrm{d}s(\mathbf{x}) = \overline{G}_{nm}(\mathbf{x}_s,\mathbf{x}_t). \quad (10)$$

Similarly, $\overline{\mathbf{G}_m(\mathbf{x},\mathbf{x}_t)}$, $m = 1,2,3$ satisfies

$$\operatorname{curl}\operatorname{curl} \overline{\mathbf{G}_m(\mathbf{x},\mathbf{x}_t)} - k^2 \overline{\mathbf{G}_m(\mathbf{x},\mathbf{x}_t)} = \delta(\mathbf{x}-\mathbf{x}_t)\mathbf{e}_m,$$

and dot-multiplying both sides with $\mathbf{G}_n(\mathbf{x},\mathbf{x}_s)$, $n = 1,2,3$ gives

$$\operatorname{curl}\operatorname{curl} \overline{\mathbf{G}_m(\mathbf{x},\mathbf{x}_t)} \cdot \mathbf{G}_n(\mathbf{x},\mathbf{x}_s) - k^2 \overline{\mathbf{G}_m(\mathbf{x},\mathbf{x}_t)} \cdot \mathbf{G}_n(\mathbf{x},\mathbf{x}_s) = \delta(\mathbf{x}-\mathbf{x}_t)\mathbf{e}_m \cdot \mathbf{G}_n(\mathbf{x},\mathbf{x}_s).$$

Integrating by part over Ω_h with respect to $\mathbf{x}$ leads to

$$\int_{\Omega_h} \operatorname{curl} \overline{\mathbf{G}_m(\mathbf{x},\mathbf{x}_t)} \cdot \operatorname{curl} \mathbf{G}_n(\mathbf{x},\mathbf{x}_s)\, \mathrm{d}\mathbf{x} - k^2 \int_{\Omega_h} \overline{\mathbf{G}_m(\mathbf{x},\mathbf{x}_t)} \cdot \mathbf{G}_n(\mathbf{x},\mathbf{x}_s)\, \mathrm{d}\mathbf{x} + \int_{\partial\Omega_h} \nu(\mathbf{x}) \times \operatorname{curl} \overline{\mathbf{G}_m(\mathbf{x},\mathbf{x}_t)} \cdot \mathbf{G}_n(\mathbf{x},\mathbf{x}_s)\, \mathrm{d}s(\mathbf{x}) = G_{mn}(\mathbf{x}_t,\mathbf{x}_s). \quad (11)$$

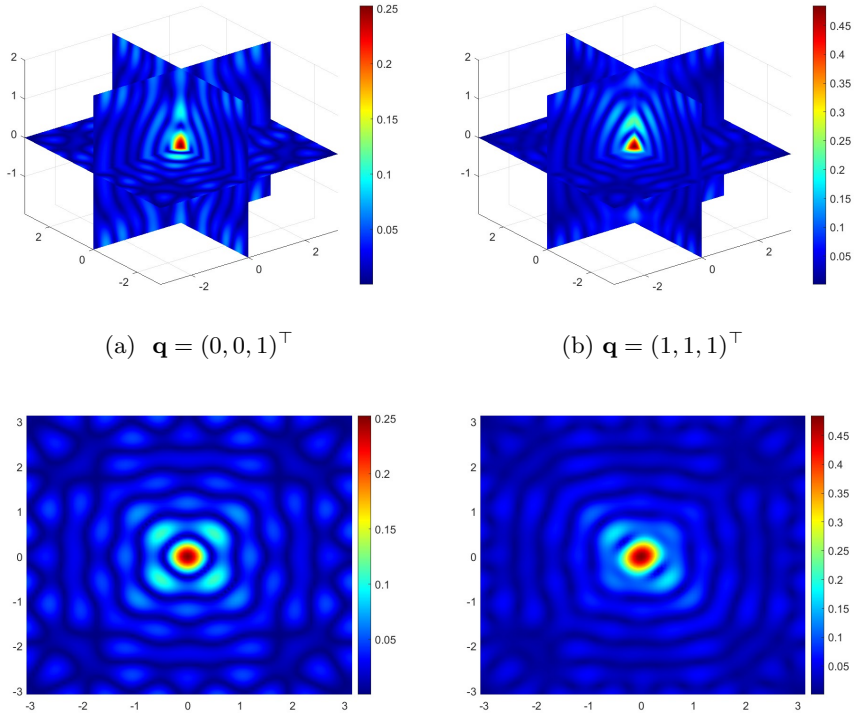

(a) $\mathbf{q} = (0, 0, 1)^\top$ (b) $\mathbf{q} = (1, 1, 1)^\top$

(c) Top view of (a) (d) Top view of (b)

Figure 2: $|\mathbb{F}(\mathbf{x}, 0)\mathbf{q}|_2$ for different vectors $\mathbf{q}$, $k = 2\pi$, $\alpha_1 = \alpha_2 = 0$.

Subtracting (10) from (11) we obtain

$$\int_{\partial\Omega_h} \nu(\mathbf{x}) \times \operatorname{curl} \overline{\mathbf{G}_m(\mathbf{x}, \mathbf{x}_t)} \cdot \mathbf{G}_n(\mathbf{x}, \mathbf{x}_s) - \nu(\mathbf{x}) \times \operatorname{curl} \mathbf{G}_n(\mathbf{x}, \mathbf{x}_s) \cdot \overline{\mathbf{G}_m(\mathbf{x}, \mathbf{x}_t)} \, \mathrm{d}s(\mathbf{x}) \\ = G_{mn}(\mathbf{x}_t, \mathbf{x}_s) - \overline{G_{nm}(\mathbf{x}_s, \mathbf{x}_t)},$$

or in matrix form

$$\int_{\partial\Omega_h} (\nu(\mathbf{x}) \times \operatorname{curl} \mathbb{G}(\mathbf{x}, \mathbf{x}_t))^* \mathbb{G}(\mathbf{x}, \mathbf{x}_s) - \mathbb{G}(\mathbf{x}, \mathbf{x}_t)^* \nu(\mathbf{x}) \times \operatorname{curl} \mathbb{G}(\mathbf{x}, \mathbf{x}_s) \, \mathrm{d}s(\mathbf{x}) \\ = \mathbb{G}(\mathbf{x}_t, \mathbf{x}_s) - \mathbb{G}^*(\mathbf{x}_s, \mathbf{x}_t), \tag{12}$$

where curl and $\times$ are taken columnwise. Since $\mathbb{G}$ is α-quasiperiodic, the integral on the left-hand side can be taken on just $\Gamma_{+h} \cup \Gamma_{-h}$. Recall from Lemma 1 that the columns of $\mathbb{G}(\cdot, \mathbf{y})$ satisfy the Rayleigh radiation condition. Letting

$$\phi_j^{\pm}(\mathbf{x}) := e^{i(\alpha_{1,j} x_1 + \alpha_{2,j} x_2 \pm \beta_j (x_3 \mp h))},$$

we compute

$$\begin{aligned}
&\int_{\Gamma_{\pm h}} (\nu(\mathbf{x}) \times \operatorname{curl} \mathbb{G}(\mathbf{x}, \mathbf{x}_t))^* \mathbb{G}(\mathbf{x}, \mathbf{x}_s) - \mathbb{G}(\mathbf{x}, \mathbf{x}_t)^* \nu(\mathbf{x}) \times \operatorname{curl} \mathbb{G}(\mathbf{x}, \mathbf{x}_s) \, \mathrm{d}s(\mathbf{x}) \\
&= \int_{\Gamma_{\pm h}} \left(\begin{bmatrix} 0 \\ 0 \\ \pm 1 \end{bmatrix} \times \sum_{j \in \mathbb{Z}^2} \operatorname{curl} \left[\mathbf{g}_j^{\pm}(\mathbf{x}_t) \phi_j^{\pm}(\mathbf{x}) \right] \right)^* \sum_{j \in \mathbb{Z}^2} \mathbf{g}_j^{\pm}(\mathbf{x}_s) \phi_j^{\pm}(\mathbf{x}) \, \mathrm{d}s(\mathbf{x}) \\
&- \int_{\Gamma_{\pm h}} \left(\sum_{j \in \mathbb{Z}^2} \mathbf{g}_j^{\pm}(\mathbf{x}_t) \phi_j^{\pm}(\mathbf{x}) \right)^* \begin{bmatrix} 0 \\ 0 \\ \pm 1 \end{bmatrix} \times \sum_{j \in \mathbb{Z}^2} \operatorname{curl} \left[\mathbf{g}_j^{\pm}(\mathbf{x}_s) \phi_j^{\pm}(\mathbf{x}) \right] \, \mathrm{d}s(\mathbf{x}).
\end{aligned}$$

For any matrix $\mathbf{A}$ (independent of $\mathbf{x}$), we obtain from a direct calculation that

$$\begin{aligned}
\operatorname{curl} \left[\mathbf{A} \phi_j^{\pm}(\mathbf{x}) \right] &= i \begin{bmatrix} a_{31}\alpha_{1,j} \mp a_{21}\beta_j & a_{32}\alpha_{1,j} \mp a_{22}\beta_j & a_{33}\alpha_{1,j} \mp a_{23}\beta_j \\ \pm a_{11}\beta_j - a_{31}\alpha_{1,j} & \pm a_{12}\beta_j - a_{32}\alpha_{1,j} & \pm a_{13}\beta_j - a_{33}\alpha_{1,j} \\ a_{21}\alpha_{1,j} - a_{11}\alpha_{2,j} & a_{22}\alpha_{1,j} - a_{12}\alpha_{2,j} & a_{23}\alpha_{1,j} - a_{13}\alpha_{2,j} \end{bmatrix} \phi_j^{\pm}(\mathbf{x}) \\
&= \left(i \begin{bmatrix} \alpha_{1,j} \\ \alpha_{2,j} \\ \pm \beta_j \end{bmatrix} \times \mathbf{A} \right) \phi_j^{\pm}(\mathbf{x}).
\end{aligned}$$

Hence,

$$\begin{aligned}
&\int_{\Gamma_{\pm h}} (\nu(\mathbf{x}) \times \operatorname{curl} \mathbb{G}(\mathbf{x}, \mathbf{x}_t))^* \mathbb{G}(\mathbf{x}, \mathbf{x}_s) - \mathbb{G}(\mathbf{x}, \mathbf{x}_t)^* \nu(\mathbf{x}) \times \operatorname{curl} \mathbb{G}(\mathbf{x}, \mathbf{x}_s) \, \mathrm{d}s(\mathbf{x}) \\
&= \int_{\Gamma_{\pm h}} \sum_{j \in \mathbb{Z}^2} \left(\begin{bmatrix} 0 \\ 0 \\ \pm 1 \end{bmatrix} \times \left(i \begin{bmatrix} \alpha_{1,j} \\ \alpha_{2,j} \\ \pm \beta_j \end{bmatrix} \times \mathbf{g}_j^{\pm}(\mathbf{x}_t) \right) \right)^* \overline{\phi_j^{\pm}(\mathbf{x})} \sum_{j \in \mathbb{Z}^2} \mathbf{g}_j^{\pm}(\mathbf{x}_s) \phi_j^{\pm}(\mathbf{x}) \, \mathrm{d}s(\mathbf{x}) \\
&- \int_{\Gamma_{\pm h}} \sum_{j \in \mathbb{Z}^2} \mathbf{g}_j^{\pm}(\mathbf{x}_t)^* \overline{\phi_j^{\pm}(\mathbf{x})} \sum_{j \in \mathbb{Z}^2} \left(\begin{bmatrix} 0 \\ 0 \\ \pm 1 \end{bmatrix} \times \left(i \begin{bmatrix} \alpha_{1,j} \\ \alpha_{2,j} \\ \pm \beta_j \end{bmatrix} \times \mathbf{g}_j^{\pm}(\mathbf{x}_s) \right) \right) \phi_j^{\pm}(\mathbf{x}) \, \mathrm{d}s(\mathbf{x}).
\end{aligned}$$

Note that the Rayleigh series in the integrand converge absolutely almost everywhere $\Gamma_{\pm h}$, thus they are bounded above by constants on the bounded set $\Gamma_{\pm h}$. By dominated convergence theorem,

$$\begin{aligned}
&\int_{\Gamma_{\pm h}} (\nu(\mathbf{x}) \times \operatorname{curl} \mathbb{G}(\mathbf{x}, \mathbf{x}_t))^* \mathbb{G}(\mathbf{x}, \mathbf{x}_s) - \mathbb{G}(\mathbf{x}, \mathbf{x}_t)^* \nu(\mathbf{x}) \times \operatorname{curl} \mathbb{G}(\mathbf{x}, \mathbf{x}_s) \, \mathrm{d}s(\mathbf{x}) \\
&= \sum_{j \in \mathbb{Z}^2} \sum_{j' \in \mathbb{Z}^2} \left(\begin{bmatrix} 0 \\ 0 \\ \pm 1 \end{bmatrix} \times \left(i \begin{bmatrix} \alpha_{1,j} \\ \alpha_{2,j} \\ \pm \beta_j \end{bmatrix} \times \mathbf{g}_j^{\pm}(\mathbf{x}_t) \right) \right)^* \mathbf{g}_{j'}^{\pm}(\mathbf{x}_s) \int_{\Gamma_{\pm h}} \phi_{j'}^{\pm}(\mathbf{x}) \overline{\phi_j^{\pm}(\mathbf{x})} \, \mathrm{d}s(\mathbf{x}) \\
&- \sum_{j \in \mathbb{Z}^2} \sum_{j' \in \mathbb{Z}^2} \mathbf{g}_j^{\pm}(\mathbf{x}_t)^* \left(\begin{bmatrix} 0 \\ 0 \\ \pm 1 \end{bmatrix} \times \left(i \begin{bmatrix} \alpha_{1,j'} \\ \alpha_{2,j'} \\ \pm \beta_{j'} \end{bmatrix} \times \mathbf{g}_{j'}^{\pm}(\mathbf{x}_s) \right) \right) \int_{\Gamma_{\pm h}} \phi_{j'}^{\pm}(\mathbf{x}) \overline{\phi_j^{\pm}(\mathbf{x})} \, \mathrm{d}s(\mathbf{x}).
\end{aligned}$$

Note that using

$$\int_{\Gamma_{\pm h}} \phi_{j'}^{\pm}(\mathbf{x}) \overline{\phi_j^{\pm}(\mathbf{x})} \, \mathrm{d}s(\mathbf{x}) = \begin{cases} 4\pi^2 & \text{if } j = j', \\ 0 & \text{if } j \neq j', \end{cases}$$

we have

$$
\begin{aligned}
&\int_{\Gamma_{\pm h}} (\nu(\mathbf{x}) \times \operatorname{curl} \mathbb{G}(\mathbf{x}, \mathbf{x}_t))^* \mathbb{G}(\mathbf{x}, \mathbf{x}_s) - \mathbb{G}(\mathbf{x}, \mathbf{x}_t)^* \nu(\mathbf{x}) \times \operatorname{curl} \mathbb{G}(\mathbf{x}, \mathbf{x}_s) \, \mathrm{d}s(\mathbf{x}) \\
&= 4\pi^2 \sum_{j \in \mathbb{Z}^2} \left(\left(\begin{bmatrix} 0 \\ 0 \\ \pm 1 \end{bmatrix} \times \left(i \begin{bmatrix} \alpha_{1,j} \\ \alpha_{2,j} \\ \pm \beta_j \end{bmatrix} \times \mathbf{g}_j^{\pm}(\mathbf{x}_t) \right) \right)^* \mathbf{g}_j^{\pm}(\mathbf{x}_s) \right. \\
&\left. - \mathbf{g}_j^{\pm}(\mathbf{x}_t)^* \left(\begin{bmatrix} 0 \\ 0 \\ \pm 1 \end{bmatrix} \times \left(i \begin{bmatrix} \alpha_{1,j} \\ \alpha_{2,j} \\ \pm \beta_j \end{bmatrix} \times \mathbf{g}_j^{\pm}(\mathbf{x}_s) \right) \right) \right) \\
&= -i4\pi^2 \sum_{j \in \mathbb{Z}^2} \left(\left(\pm \mathbf{h}_j^{\pm}(\mathbf{x}_t) - \beta_j \mathbf{g}_j^{\pm}(\mathbf{x}_t) \right)^* \mathbf{g}_j^{\pm}(\mathbf{x}_s) + \mathbf{g}_j^{\pm}(\mathbf{x}_t)^* \left(\pm \mathbf{h}_j^{\pm}(\mathbf{x}_s) - \beta_j \mathbf{g}_j^{\pm}(\mathbf{x}_s) \right) \right) \\
&= -i4\pi^2 \sum_{j \in \mathbb{Z}^2} \left(\left(\pm \mathbf{h}_j^{\pm}(\mathbf{x}_t) - 2\mathrm{Re}\,(\beta_j)\ \mathbf{g}_j^{\pm}(\mathbf{x}_t) \right)^* \mathbf{g}_j^{\pm}(\mathbf{x}_s) \pm \mathbf{g}_j^{\pm}(\mathbf{x}_t)^* \mathbf{h}_j^{\pm}(\mathbf{x}_s) \right).
\end{aligned}
$$

Therefore we obtain that

$$
\begin{aligned}
&\int_{\partial\Omega_h} (\nu(\mathbf{x}) \times \operatorname{curl} \mathbb{G}(\mathbf{x}, \mathbf{x}_t))^* \mathbb{G}(\mathbf{x}, \mathbf{x}_s) - \mathbb{G}(\mathbf{x}, \mathbf{x}_t)^* \nu(\mathbf{x}) \times \operatorname{curl} \mathbb{G}(\mathbf{x}, \mathbf{x}_s) \mathrm{d}s(\mathbf{x}) \\
&= -i4\pi^2 \sum_{j \in \mathbb{Z}^2} \left(\left(\mathbf{h}_j^{+}(\mathbf{x}_t) - 2\mathrm{Re}\,(\beta_j)\ \mathbf{g}_j^{+}(\mathbf{x}_t) \right)^* \mathbf{g}_j^{+}(\mathbf{x}_s) + \mathbf{g}_j^{+}(\mathbf{x}_t)^* \mathbf{h}_j^{+}(\mathbf{x}_s) \right. \\
&\qquad \left. - \left(\mathbf{h}_j^{-}(\mathbf{x}_t) + 2\mathrm{Re}\,(\beta_j)\ \mathbf{g}_j^{-}(\mathbf{x}_t) \right)^* \mathbf{g}_j^{-}(\mathbf{x}_s) - \mathbf{g}_j^{-}(\mathbf{x}_t)^* \mathbf{h}_j^{-}(\mathbf{x}_s) \right). \qquad (13)
\end{aligned}
$$

Now recall that the scattered field $\mathbf{u}(\mathbf{x}, l)$ satisfies

$$
\mathbf{u}(\mathbf{x}, l) = (k^2 + \nabla_{\mathbf{x}} \mathrm{div}_{\mathbf{x}}) \int_D \Phi(\mathbf{x}, \mathbf{y})(\varepsilon(\mathbf{y}) - I_3)\mathbf{E}(\mathbf{y}, l) \, \mathrm{d}\mathbf{y}.
$$

Thus by (5),

$$
\mathbf{u}_j^{\pm}(l) = \frac{1}{4\pi^2} \int_{\Gamma_{\pm h}} \int_D (k^2 + \nabla_{\mathbf{x}} \mathrm{div}_{\mathbf{x}}) \left(\Phi(\mathbf{x}, \mathbf{y})(\varepsilon(\mathbf{y}) - I_3)\mathbf{E}(\mathbf{y}, l) \right) \mathrm{d}\mathbf{y} \ e^{-i(\alpha_{1,j} x_1 + \alpha_{2,j} x_2 \pm \beta_j (x_3 \mp h))} \mathrm{d}s(\mathbf{x}).
$$

For $\mathbf{x} \in \Gamma_{\pm h}$ and $\mathbf{y} \in D$, the integrand is bounded on the bounded sets $\Gamma_{\pm h} \times D$, thus, by Fubini's theorem,

$$
\begin{aligned}
\mathbf{u}_j^{\pm}(l) &= k^2 \int_D \frac{1}{4\pi^2} \int_{\Gamma_{\pm h}} \mathbb{G}(\mathbf{x}, \mathbf{y}) e^{-i(\alpha_{1,j} x_1 + \alpha_{2,j} x_2 \pm \beta_j (x_3 \mp h))} \mathrm{d}s(\mathbf{x}) \left(\varepsilon(\mathbf{y}) - I_3 \right) \mathbf{E}(\mathbf{y}, l) \, \mathrm{d}\mathbf{y} \\
&= k^2 \int_D \mathbf{g}_j^{\pm}(\mathbf{y})(\varepsilon(\mathbf{y}) - I_3)\mathbf{E}(\mathbf{y}, l) \, \mathrm{d}\mathbf{y}, \qquad (14)
\end{aligned}
$$

and so

$$\begin{aligned}
\begin{bmatrix}\alpha_{1,j}\\ \alpha_{2,j}\\ \pm\beta_j\end{bmatrix} u^{\pm}_{3,j}(l) &= k^2 \begin{bmatrix}\alpha_{1,j}\\ \alpha_{2,j}\\ \pm\beta_j\end{bmatrix} \int_D \begin{bmatrix}(g^{\pm}_{31})_j & (g^{\pm}_{32})_j & (g^{\pm}_{33})_j\end{bmatrix}(\mathbf{y})(\varepsilon(\mathbf{y})-I_3)\mathbf{E}(\mathbf{y},l)\,\mathrm{d}\mathbf{y}\\
&= k^2 \int_D \begin{bmatrix}\alpha_{1,j}(g^{\pm}_{31})_j & \alpha_{1,j}(g^{\pm}_{32})_j & \alpha_{1,j}(g^{\pm}_{33})_j\\ \alpha_{2,j}(g^{\pm}_{31})_j & \alpha_{2,j}(g^{\pm}_{32})_j & \alpha_{2,j}(g^{\pm}_{33})_j\\ \pm\beta_j(g^{\pm}_{31})_j & \pm\beta_j(g^{\pm}_{32})_j & \pm\beta_j(g^{\pm}_{33})_j\end{bmatrix}(\varepsilon(\mathbf{y})-I_3)\mathbf{E}(\mathbf{y},l)\,\mathrm{d}\mathbf{y}\\
&= k^2 \int_D \mathbf{h}^{\pm}_j(\mathbf{y})(\varepsilon(\mathbf{y})-I_3)\mathbf{E}(\mathbf{y},l)\,\mathrm{d}\mathbf{y}. \qquad (15)
\end{aligned}$$

Now recall that, for $\mathbf{z}\in\Omega_h$,

$$\begin{aligned}
\mathcal{I}(\mathbf{z}) = \sum_{l=1}^{N}\Bigg|\sum_{j\in\mathbb{Z}^2}\Bigg(&\Big(\mathbf{h}^+_j(\mathbf{z}) - 2\mathrm{Re}\,(\beta_j)\ \mathbf{g}^+_j(\mathbf{z})\Big)^*\mathbf{u}^+_j(l) + u^+_{3,j}(l)\mathbf{g}^+_j(\mathbf{z})^*\begin{bmatrix}\alpha_{1,j}\\ \alpha_{2,j}\\ \beta_j\end{bmatrix}\\
&-\Big(\mathbf{h}^-_j(\mathbf{z}) + 2\mathrm{Re}\,(\beta_j)\ \mathbf{g}^-_j(\mathbf{z})\Big)^*\mathbf{u}^-_j(l) - u^-_{3,j}(l)\mathbf{g}^-_j(\mathbf{z})^*\begin{bmatrix}\alpha_{1,j}\\ \alpha_{2,j}\\ -\beta_j\end{bmatrix}\Bigg)\Bigg|^p.
\end{aligned}$$

Plugging the formula of $\mathbf{u}^{\pm}_j(l)$ and $[\alpha_{1,j}\ \alpha_{2,j}\ \pm\beta_j]^\top u^{\pm}_{3,j}(l)$ in (14) and (15) into $\mathcal{I}(\mathbf{z})$ and using identities (12) and (13), we obtain that

$$\mathcal{I}(\mathbf{z}) = \sum_{l=1}^{N}\left|\frac{k^2}{2\pi^2}\int_D \frac{1}{2i}\left(\mathbb{G}(\mathbf{z},\mathbf{y})-\mathbb{G}^*(\mathbf{y},\mathbf{z})\right)(\varepsilon(\mathbf{y})-I_3)\mathbf{E}(\mathbf{y},l)\,\mathrm{d}\mathbf{y}\right|^p.$$

Now letting

$$F(\mathbf{x},\mathbf{y}) := \frac{1}{2i}\left(\Phi(\mathbf{x},\mathbf{y}) - \overline{\Phi(\mathbf{y},\mathbf{x})}\right),$$

a direct calculation leads to

$$\mathbb{F}(\mathbf{x},\mathbf{y}) := \frac{1}{2i}(\mathbb{G}(\mathbf{x},\mathbf{y})-\mathbb{G}^*(\mathbf{y},\mathbf{x})) = F(\mathbf{x},\mathbf{y})I_3 + \frac{1}{k^2}\nabla\mathrm{div}(F(\mathbf{x},\mathbf{y})I_3).$$

The proof follows from using the following expression of the scalar α-quasiperiodic Green's function $\Phi(\mathbf{x},\mathbf{y})$, see e.g. [3],

$$\Phi(\mathbf{x},\mathbf{y}) = \sum_{j\in\mathbb{Z}^2} e^{-i2\pi\alpha\cdot j}\frac{e^{ik\sqrt{(x_1-y_1+2j_1\pi)^2+(x_2-y_2+2j_2\pi)^2+(x_3-y_3)^2}}}{4\pi\sqrt{(x_1-y_1+2j_1\pi)^2+(x_2-y_2+2j_2\pi)^2+(x_3-y_3)^2}},$$

for $\mathbf{x},\mathbf{y}\in\Omega_h$ such that $x_3\neq y_3$. □

Denote by $|\cdot|_F$ and $|\cdot|_2$ the Frobenius norm of a matrix and the 2-norm of a vector, respectively. In the next theorem we analyze the stability of the imaging functional.

Theorem 5. *For $\delta>0$, let $\mathbf{u}^\delta$ be the noisy data such that*

$$\left\|\mathbf{u}^\delta(\cdot,l)-\mathbf{u}(\cdot,l)\right\|_{L^2(\Gamma_h\cup\Gamma_{-h})}\leq\delta,\quad \forall l=1,2,\ldots,N,$$

and let $\mathcal{I}_\delta$ be the imaging functional computed from this noisy data. Then, there exists a constant $C>0$ independent of $\mathbf{z}$ and δ such that, for all $\mathbf{z}\in\Omega_h$,

$$|\mathcal{I}_\delta(\mathbf{z})-\mathcal{I}(\mathbf{z})|\leq C\delta,\quad \text{as } \delta\to 0.$$

Proof. Note that, for all $j \in \mathbb{Z}^2$ and $l = 1, \ldots, N$,

$$\left|\mathbf{u}^{\pm}_{\delta,j}(l) - \mathbf{u}^{\pm}_{j}(l)\right|_2 \leq \frac{1}{4\pi^2} \int_{\Gamma_{\pm h}} \left|\mathbf{u}^{\delta}(\mathbf{x}, l) - \mathbf{u}(\mathbf{x}, l)\right| \, \mathrm{d}s(\mathbf{x}).$$

Thus, by Cauchy-Schwarz inequality,

$$\left|\mathbf{u}^{\pm}_{\delta,j}(l) - \mathbf{u}^{\pm}_{j}(l)\right|_2 \leq \left\|\mathbf{u}^{\delta}(\cdot, l) - \mathbf{u}(\cdot, l)\right\|_{L^2(\Gamma_{\pm h})} \leq \delta.$$

Fix $\mathbf{z} \in \Omega_h$ and $\delta > 0$. For $l = 1, 2, \ldots, N$, let

$$A_l := \left| \sum_{j \in \mathbb{Z}^2} \left(\left(\mathbf{h}^+_j(\mathbf{z}) - 2\mathrm{Re}\,(\beta_j)\ \mathbf{g}^+_j(\mathbf{z}) \right)^* \mathbf{u}^+_{\delta,j}(l) + u^+_{\delta,3,j}(l) \mathbf{g}^+_j(\mathbf{z})^* \begin{bmatrix} \alpha_{1,j} \\ \alpha_{2,j} \\ \beta_j \end{bmatrix} \right. \right.$$
$$\left. \left. - \left(\mathbf{h}^-_j(\mathbf{z}) + 2\mathrm{Re}\,(\beta_j)\ \mathbf{g}^-_j(\mathbf{z}) \right)^* \mathbf{u}^-_{\delta,j}(l) - u^-_{\delta,3,j}(l) \mathbf{g}^-_j(\mathbf{z})^* \begin{bmatrix} \alpha_{1,j} \\ \alpha_{2,j} \\ -\beta_j \end{bmatrix} \right) \right|,$$

and

$$B_l := \left| \sum_{j \in \mathbb{Z}^2} \left(\left(\mathbf{h}^+_j(\mathbf{z}) - 2\mathrm{Re}\,(\beta_j)\ \mathbf{g}^+_j(\mathbf{z}) \right)^* \mathbf{u}^+_{j}(l) + u^+_{3,j}(l) \mathbf{g}^+_j(\mathbf{z})^* \begin{bmatrix} \alpha_{1,j} \\ \alpha_{2,j} \\ \beta_j \end{bmatrix} \right. \right.$$
$$\left. \left. - \left(\mathbf{h}^-_j(\mathbf{z}) + 2\mathrm{Re}\,(\beta_j)\ \mathbf{g}^-_j(\mathbf{z}) \right)^* \mathbf{u}^-_{j}(l) - u^-_{3,j}(l) \mathbf{g}^-_j(\mathbf{z})^* \begin{bmatrix} \alpha_{1,j} \\ \alpha_{2,j} \\ -\beta_j \end{bmatrix} \right) \right|,$$

it is then clear that

$$\mathcal{I}_\delta(\mathbf{z}) = \sum_{l=1}^{N} A^p_l \quad \text{and} \quad \mathcal{I}(\mathbf{z}) = \sum_{l=1}^{N} B^p_l.$$

Using the Cauchy-Schwarz inequality and the triangle inequality, we estimate

$$\begin{aligned} |A_l - B_l| &\leq \sum_{j \in \mathbb{Z}^2} \left|\mathbf{u}^+_{\delta,j}(l) - \mathbf{u}^+_j(l)\right|_2 \left(\left|\mathbf{h}^+_j(\mathbf{z})\right|_F + 2\mathrm{Re}\,(\beta_j) \left|\mathbf{g}^+_j(\mathbf{z})\right|_F + \left| \mathbf{g}^+_j(\mathbf{z})^* \begin{bmatrix} \alpha_{1,j} \\ \alpha_{2,j} \\ \beta_j \end{bmatrix} \right|_2 \right) \\ &\quad + \sum_{j \in \mathbb{Z}^2} \left|\mathbf{u}^-_{\delta,j}(l) - \mathbf{u}^-_j(l)\right|_2 \left(\left|\mathbf{h}^-_j(\mathbf{z})\right|_F + 2\mathrm{Re}\,(\beta_j) \left|\mathbf{g}^-_j(\mathbf{z})\right|_F + \left| \mathbf{g}^-_j(\mathbf{z})^* \begin{bmatrix} \alpha_{1,j} \\ \alpha_{2,j} \\ -\beta_j \end{bmatrix} \right|_2 \right) \\ &\leq C_1 \delta, \end{aligned}$$

where

$$C_1 := \sup_{\mathbf{z} \in \Omega_h} \sum_{j \in \mathbb{Z}^2} \left(\left|\mathbf{h}^+_j(\mathbf{z})\right|_F + \left|\mathbf{h}^-_j(\mathbf{z})\right|_F + (2\mathrm{Re}\,(\beta_j) + k) \left(\left|\mathbf{g}^+_j(\mathbf{z})\right|_F + \left|\mathbf{g}^-_j(\mathbf{z})\right|_F \right) \right).$$

Note that $C_1 < \infty$ since the sequences $\left(\sup_{\mathbf{z} \in \Omega_h} \left|\mathbf{h}^{\pm}_j(\mathbf{z})\right|_F\right)_j$ and $\left(\sup_{\mathbf{z} \in \Omega_h} \left|\mathbf{g}^{\pm}_j(\mathbf{z})\right|_F\right)_j$ quickly decay as mentioned in Remark 2. C_1 is also independent of $\mathbf{z}$ and δ. Using a similar argument, we can show that, for all $l = 1, 2, \ldots, N$,

$$B_l \leq C_1 \|\mathbf{u}(\cdot, l)\|_{L^2(\Gamma_h \cup \Gamma_{-h})}. \tag{16}$$

Next,

$$\begin{aligned}\left|A_l^p - B_l^p\right| &\le |A_l - B_l| \sum_{m=0}^{p-1} A_l^m B_l^{p-1-m} \\ &\le |A_l - B_l| \sum_{m=0}^{p-1} (|A_l - B_l| + B_l)^m B_l^{p-1-m}.\end{aligned}$$

For two nonnegative numbers a, b and $m = 0, \ldots, p-1$,

$$(a+b)^m \le (2\max\{a,b\})^m = 2^m \max\{a^m, b^m\} \le 2^m(a^m + b^m),$$

hence,

$$\begin{aligned}\left|A_l^p - B_l^p\right| &\le |A_l - B_l| \sum_{m=0}^{p-1} 2^m (|A_l - B_l|^m + B_l^m) B_l^{p-1-m} \\ &\le C_1\delta \sum_{m=0}^{p-1} 2^m (C_1^m \delta^m + B_l^m) B_l^{p-1-m}.\end{aligned}$$

Thus, when $\delta < 1$,

$$\left|A_l^p - B_l^p\right| \le C_1\delta \sum_{m=0}^{p-1} 2^m (C_1^m + B_l^m) B_l^{p-1-m}.$$

Using the estimate (16), we get

$$\left|A_l^p - B_l^p\right| \le C_1^p \delta \sum_{m=0}^{p-1} 2^m \left(1 + \|\mathbf{u}(\cdot, l)\|^m_{L^2(\Gamma_h \cup \Gamma_{-h})}\right) \|\mathbf{u}(\cdot, l)\|^{p-1-m}_{L^2(\Gamma_h \cup \Gamma_{-h})} = C_2\delta,$$

where $C_2 > 0$ is independent of $\mathbf{z}$ and δ. Therefore, as $\delta \to 0$,

$$|\mathcal{I}_\delta(\mathbf{z}) - \mathcal{I}(\mathbf{z})| \le \sum_{l=1}^{N} \left|A_l^p - B_l^p\right| \le C\delta,$$

where $C = NC_2$ is independent of $\mathbf{z}$ and δ, which completes the proof. □

We have provided justifications for the resolution and stability of the new imaging functional. In the next part, we will discuss its numerical performance.

4 Numerical study

In this section, we show numerical results for the imaging functional in the following situations.

- Different numbers of evanescent modes are used.
- Noise with different levels is added to the data.
- Different numbers of incident sources are used.

- The receivers used to measure the scattered fields are placed at different distances from the medium.
- Different values of α_1 and α_2 are used.
- The factorization method and orthogonality sampling method are used in comparison.

In the numerical simulation, we use the wave number $k = 2\pi$. The exponent of the imaging functional is $p = 3$. To simplify the calculation, we choose $\mathbf{J}(\cdot, l) = \sum_{j\in\mathbb{Z}^2}(0,0,1)^\top \delta_{\mathbf{y}_l+2\pi j}$ that means the incident fields are the third column of the Green's tensor, more specifically, they are emitted from point sources and have the form

$$\mathbf{E}^{inc}(\mathbf{x}, l) = -\frac{i}{8\pi^2 k^2}\sum_{j\in\mathbb{Z}^2}\begin{bmatrix}\mathrm{sgn}(y_3^l - x_3)\alpha_{1,j}\\ \mathrm{sgn}(y_3^l - x_3)\alpha_{2,j}\\ k^2/\beta_j + \beta_j\end{bmatrix} e^{i(\alpha_{1,j}(y_1^l - x_1)+\alpha_{2,j}(y_2^l - x_2)+\beta_j|y_3^l - x_3|)}, \quad \mathbf{x}\in\Omega_h \tag{17}$$

where $\mathbf{y}_l = (y_1^l, y_2^l, y_3^l)$ are the sources' locations and sgn is the sign function. The sources are placed evenly on two planes $(-\pi,\pi)^2 \times \{\pm 2.5\}$. Regarding the points of measurement, 3200 receivers are placed evenly on two planes $(-\pi,\pi)^2 \times \{\pm h\}$. To generate synthetic data for the inverse problem, we solve the volume integro-differential equation (9) using a spectral Galerkin method studied in [21]. We compute the scattered fields at the points of measurements, then add artificial noise with noise level $\delta > 0$. To be specific, let $\mathbf{U}$ be the matrix containing the values of the scattered fields. We create a noise matrix $\mathbf{N}$ of the same size as $\mathbf{U}$. The entries of $\mathbf{N}$ are complex numbers whose real and imaginary parts are uniformly distributed random numbers on $[-1, 1]$. The noisy version of $\mathbf{U}$ is then

$$\mathbf{U}_\delta := \mathbf{U} + \delta|\mathbf{U}|_F\frac{\mathbf{N}}{|\mathbf{N}|_F}.$$

After adding the noise, we compute the Rayleigh coefficients using (5). In all of the numerical examples, the isovalue for the 3D reconstructions is 60% of the maximum value of the imaging functional $\mathcal{I}(\mathbf{z})$. This isovalue is chosen to get the best 3D representation for the reconstructions across all examples, and is done by trial-and-error. Finally, the other parameters will vary among tests. However, unless specifically mentioned, their values are as follows.

- Number of evanescent modes used: 0.
- Noise level: 20%.
- Number of incident sources: 800.
- $h = 1$.
- $\alpha_1 = \alpha_2 = 0$.

We demonstrate the numerical performance of the imaging functional for the following types of periodic media.

1. **Ring.** This medium consists of a short hollow cylinder which resembles a ring in each period. The inner circle has radius 1 while the outer circle has radius 1.5. The height of the cylinder is 0.2. The permittivity $\varepsilon(\mathbf{x})$ is given by

$$\varepsilon(\mathbf{x}) = \begin{cases}\mathrm{diag}(1.3, 1.5, 1.4) & \text{if } \mathbf{x}\in D,\\ I_3 & \text{if } \mathbf{x}\notin D.\end{cases}$$

2. **Sphere.** This medium consists of four aligned spheres in each period. The radius of each sphere is 0.4, and the permittivity is similar to that of the ring case.

3. **Cube.** This medium consists of one cube in each period. The dimensions of each cube are $(-1,1)^2 \times (-0.3,0.3)$, and the permittivity is similar to that of the ring case.

4. **Perforated Sheet.** This medium is a sheet that contains one circular hole in each period. The radius of each hole is 1 and the thickness of the sheet is 0.6. The permittivity $\varepsilon(\mathbf{x})$ is given by

$$\varepsilon(\mathbf{x}) = \begin{cases} \text{diag}(1.03, 1.05, 1.04) & \text{if } \mathbf{x} \in D, \\ I_3 & \text{if } \mathbf{x} \notin D. \end{cases}$$

4.1 Reconstruction with different numbers of evanescent modes (Figure 3)

We have discussed the contribution of propagating and evanescent modes to the imaging functional in Remark 2. Recall that propagating modes correspond to real-valued β_j's and are finite, whereas evanescent modes correspond to complex-valued β_j's and are infinite. However, we observe that only propagating modes contribute significantly to the reconstruction, and different numbers of evanescent modes yield similar results. Figure 3 shows a comparison between two reconstructions of the ring, one using 903 evanescent modes and one using no evanescent modes. The results are very similar. We also tested with 203 evanescent modes and the result was also similar. Using only propagating modes helps reduce computational cost and avoid any instability involving evanescent modes.

4.2 Reconstruction with highly noisy data (Figure 4-5)

We have shown that the imaging functional is theoretically stable against noise in the data. Numerically, the imaging functional is not only stable but can also handle high levels of noise. In Figure 4, we show the reconstructions of the ring at noise levels $\delta = 40\%$ and $\delta = 60\%$. It can be seen that the method gives very similar results. We also compare the reconstruction with that of the factorization method. We regularize the factorization method by using singular value decomposition and truncating the singular values of the data matrix. In Figure 5, we show the reconstructions with two different random noise matrices $\mathbf{N}_1$ and $\mathbf{N}_2$, both at noise level $\delta = 20\%$. The truncation value is chosen as $\sigma = 10^{-2}$. All singular values that are smaller than σ are omitted from the reconstruction. We have tested with other truncation values as well but this one gives the best result. The factorization method cannot give as a good result as our method, and it is not stable in the sense that two different noise matrices at the same level can still lead to noticeably different reconstructions.

4.3 Reconstruction with different numbers of incident sources (Figure 6)

Generally, more incident sources means more data, and thus, means better reconstructions. However, as the number of incident sources increases, the reconstruction from the imaging functional will stop changing at some point. Figure 6 shows the reconstructions with 200 and 450 incident sources. The latter gives a better result, and the result will not change even if we increase the number of incident sources to above 450.

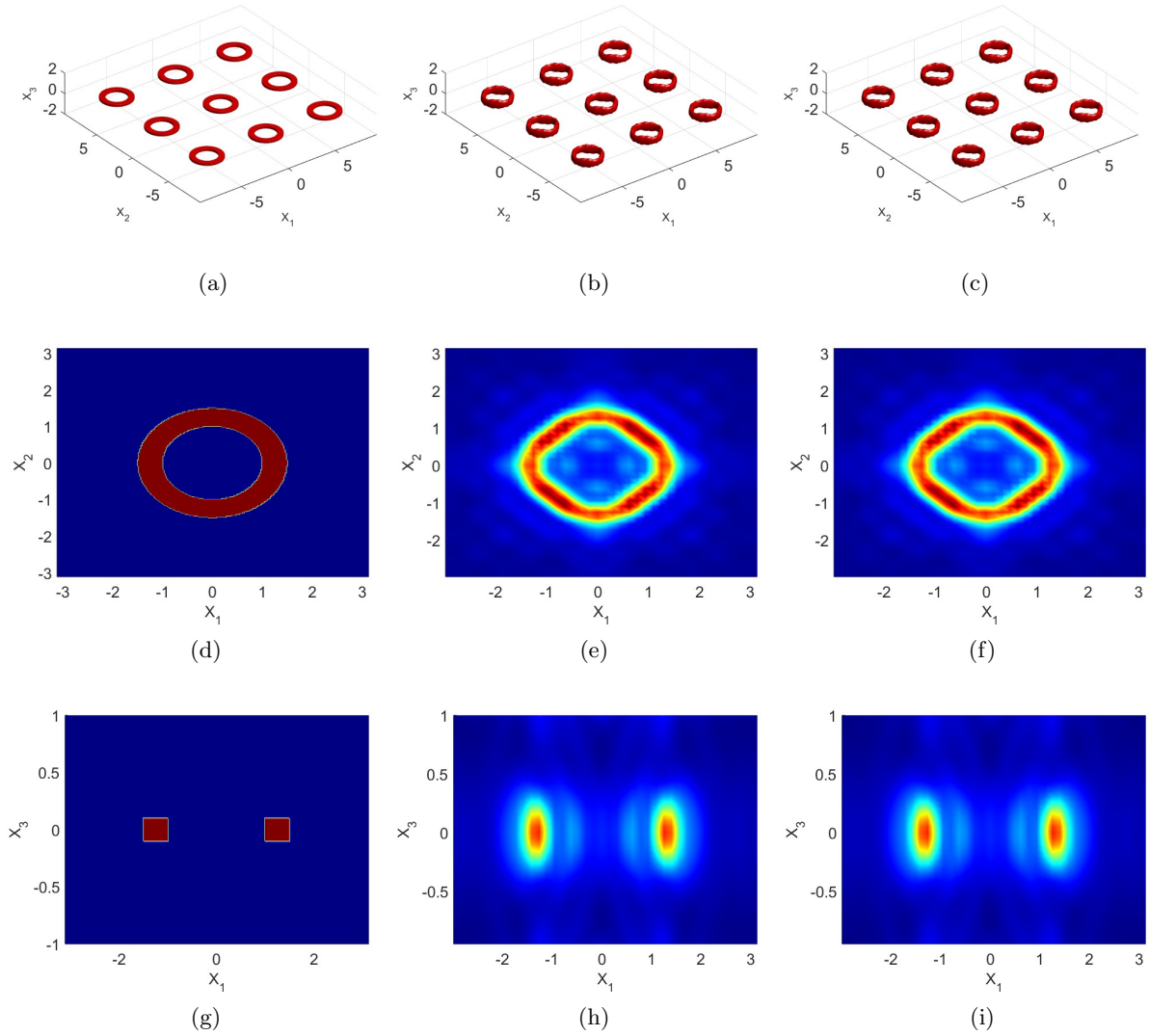

Figure 3: Reconstruction with different numbers of evanescent modes. First column (a, d, g): True geometry in 3D and 2D views. Second column (b, e, h): reconstruction with 903 evanescent modes. Third column (c, f, i): reconstruction with no evanescent modes.

4.4 Reconstruction with different distances between the medium and the receivers (Figure 7)

Recall that the receivers are evenly distributed on two planes: Γ_{+h} and Γ_{-h}, which lie above and below the medium, respectively. Figure 7 compares the reconstructions for $h = 1$ and $h = 2.5$. The two reconstructions are extremely similar. This test demonstrates that the method remains largely unaffected by the distance between the medium and the receivers, as long as the measurements fall within the near-field regime.

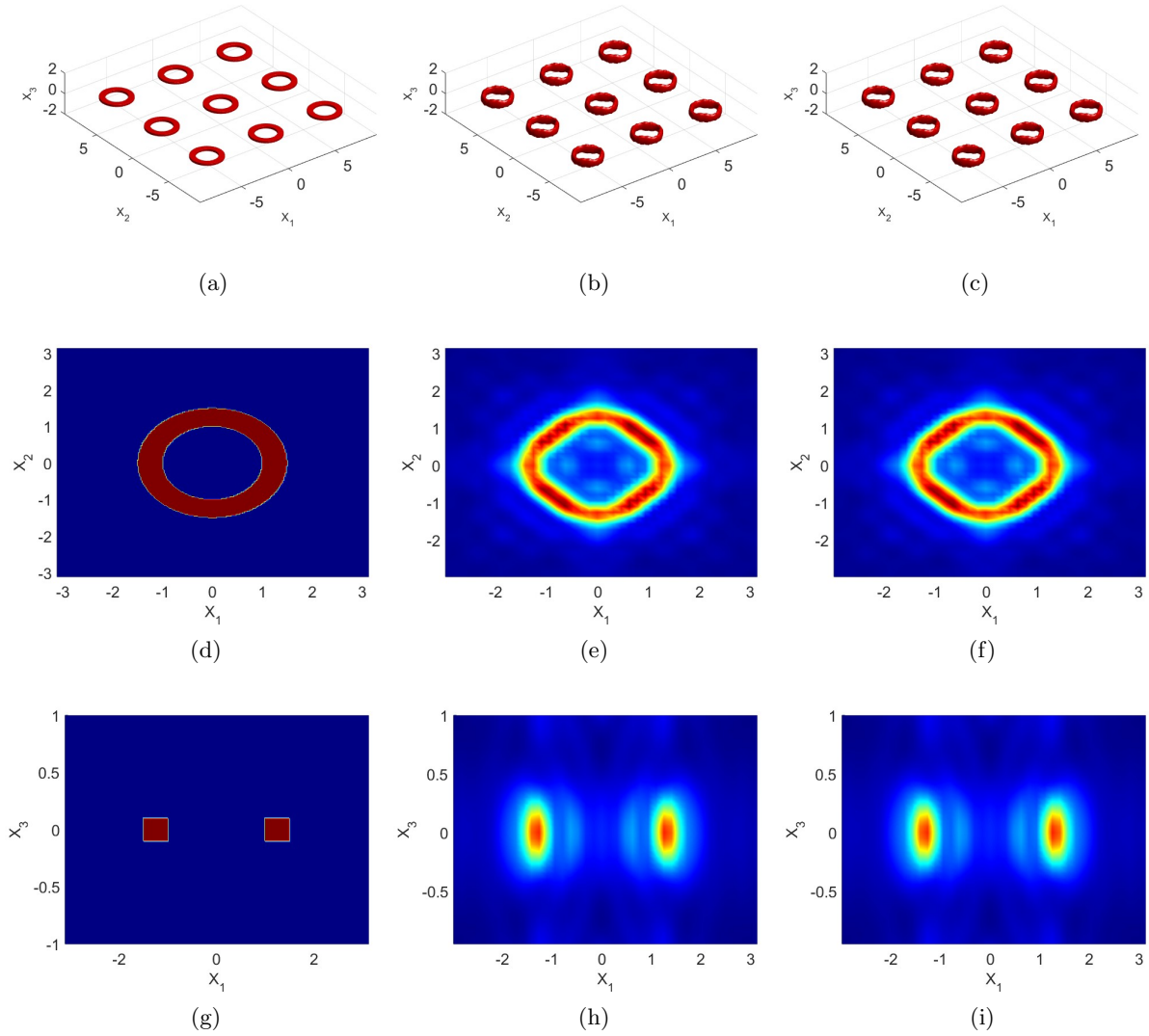

Figure 4: Reconstruction with highly noisy data. First column (a, d, g): True geometry in 3D and 2D views. Second column (b, e, h): reconstruction with 40% noise. Third column (c, f, i): reconstruction with 60% noise.

4.5 Reconstruction with different values of α_1 and α_2 (Figure 8)

The case $\alpha_1 = \alpha_2 = 0$ is the most ideal case for the imaging functional, as the kernel tensor $\mathbb{F}$ behaves very well according to Remark 4. Other values of α_1 and α_2 may slightly affect this behavior and thus affect the performance of the imaging functional. In Figure 8, we show the reconstructions of the ring in two cases, $\alpha_1 = 0$, $\alpha_2 = \pi\sqrt{2}$ and $\alpha_1 = \alpha_2 = \pi$. It can be seen that these reconstructions are slightly different from the case $\alpha_1 = \alpha_2 = 0$.

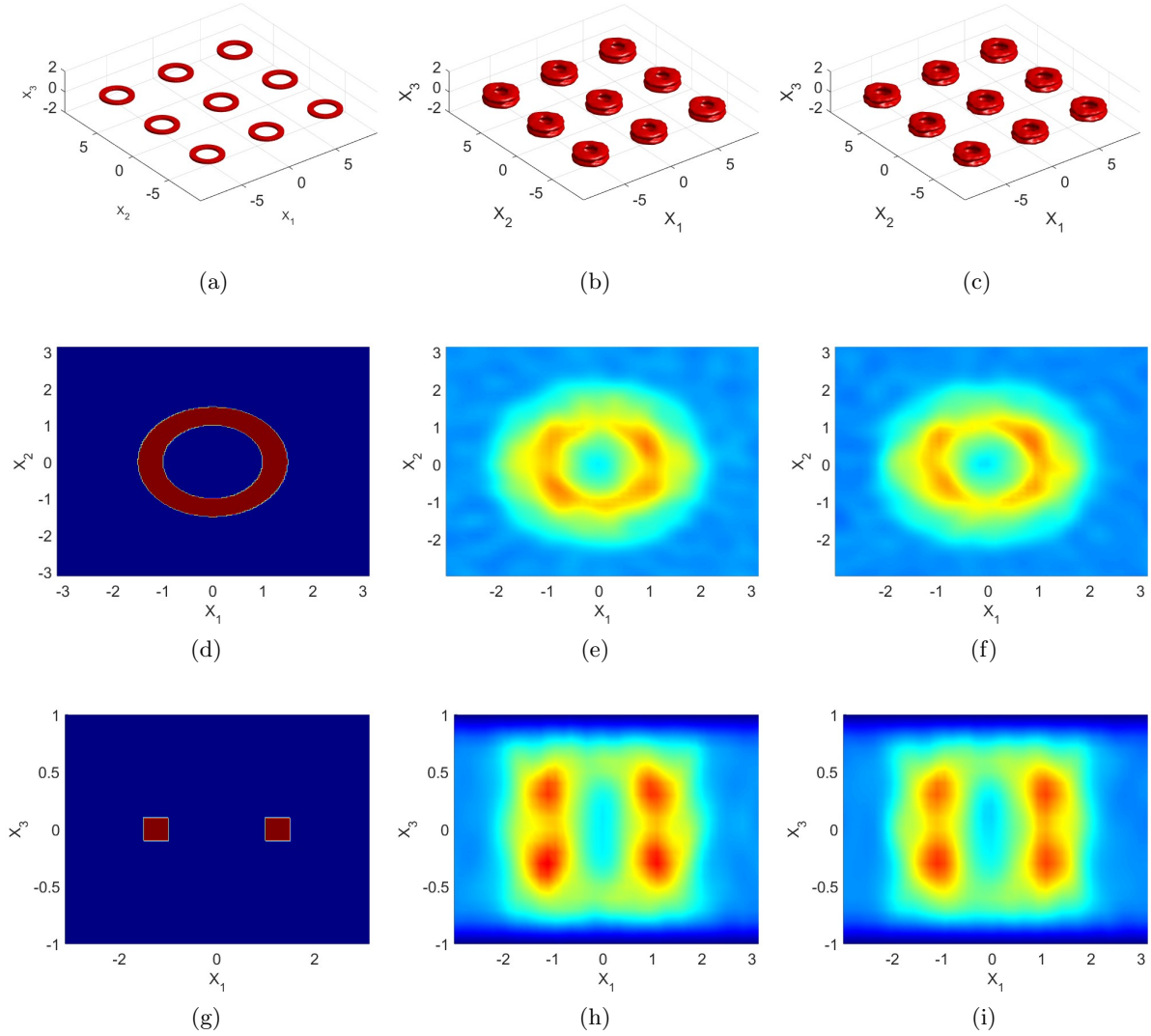

Figure 5: Reconstruction using the factorization method for the ring with two random noise matrices $\mathbf{N}_1$ and $\mathbf{N}_2$, both at 20% noise. First column (a, d, g): True geometry in 3D and 2D views. Second column (b, e, h): reconstruction with noise matrix $\mathbf{N}_1$. Third column (c, f, i): reconstruction with noise matrix $\mathbf{N}_2$.

4.6 Comparison with the orthogonality sampling method (Figures 9-12)

The orthogonality sampling method (OSM) is a well-known sampling method that has been studied extensively for the case of bounded scattering objects. In this subsection, we conduct multiple comparisons between our proposed method and the OSM. The imaging functional of the OSM is given by

$$\mathcal{I}_{\mathrm{OSM}}(\mathbf{z}) := \sum_{l=1}^{N} \left| \int_{\Gamma_h \cup \Gamma_{-h}} \mathbf{u}(\mathbf{x}, l) \cdot \mathbf{q} \overline{G(\mathbf{z}, \mathbf{x})} \, \mathrm{d}s(\mathbf{x}) \right|^p ,$$

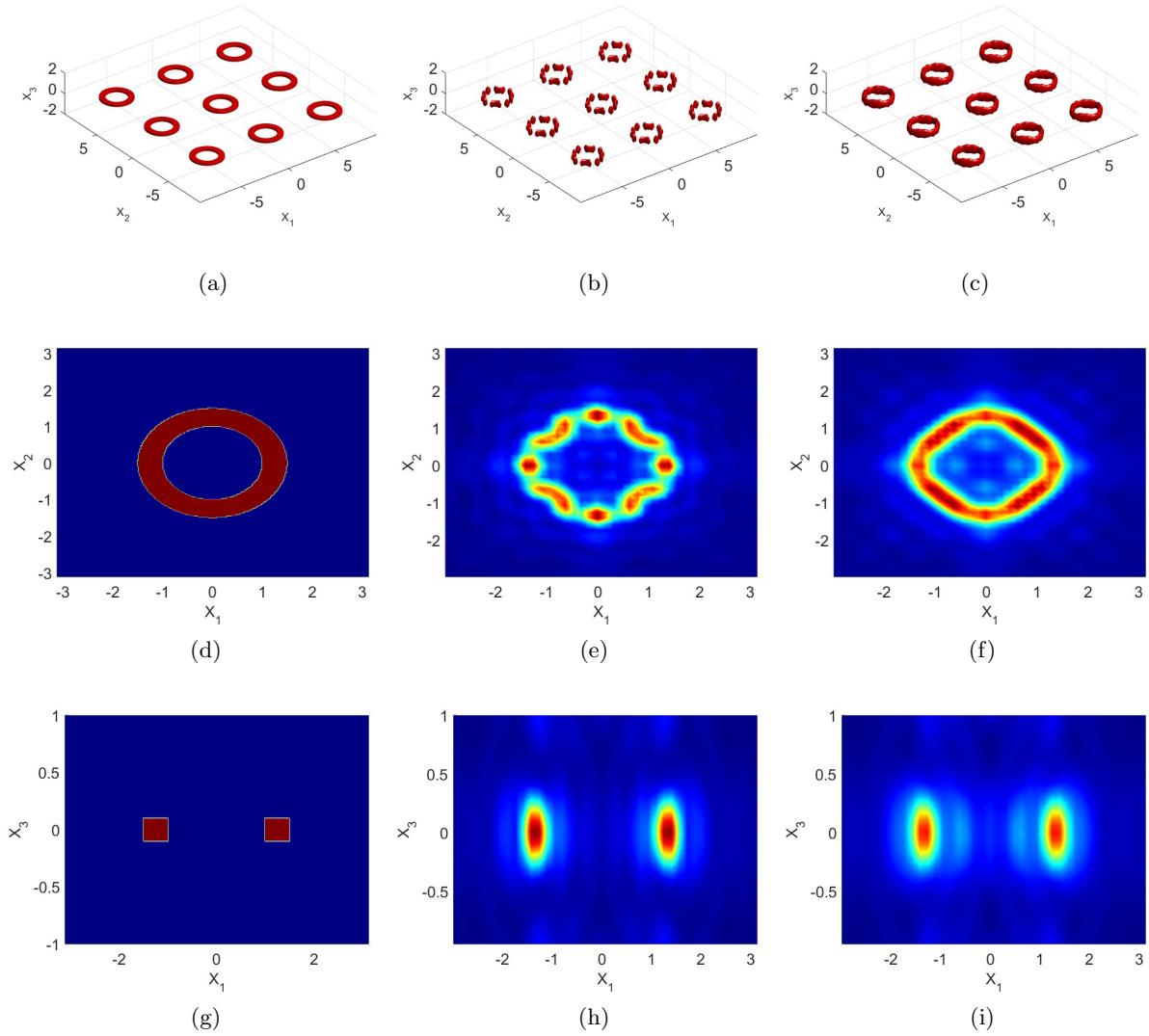

Figure 6: Reconstruction with different numbers of incident sources. First column (a, d, g): True geometry in 3D and 2D views. Second column (b, e, h): reconstruction with 200 incident sources. Third column (c, f, i): reconstruction with 450 incident sources.

where the polarization $\mathbf{q} = (1, 1, 1)^\top$ and the exponent $p = 3$. From Figures 9-11, we can see that the new sampling method method can provide better reconstructions than the OSM. The OSM is able to provide reasonable reconstructions in the x_1 and x_2 directions but not the in the x_3 direction.

5 Conclusion

We propose a sampling method with a new imaging functional for reconstructing the geometry of periodic media from electromagnetic scattering data. Its most remarkable advantage, compared to alternative approaches addressing this problem, lies in its speed, simplicity of implementation, and

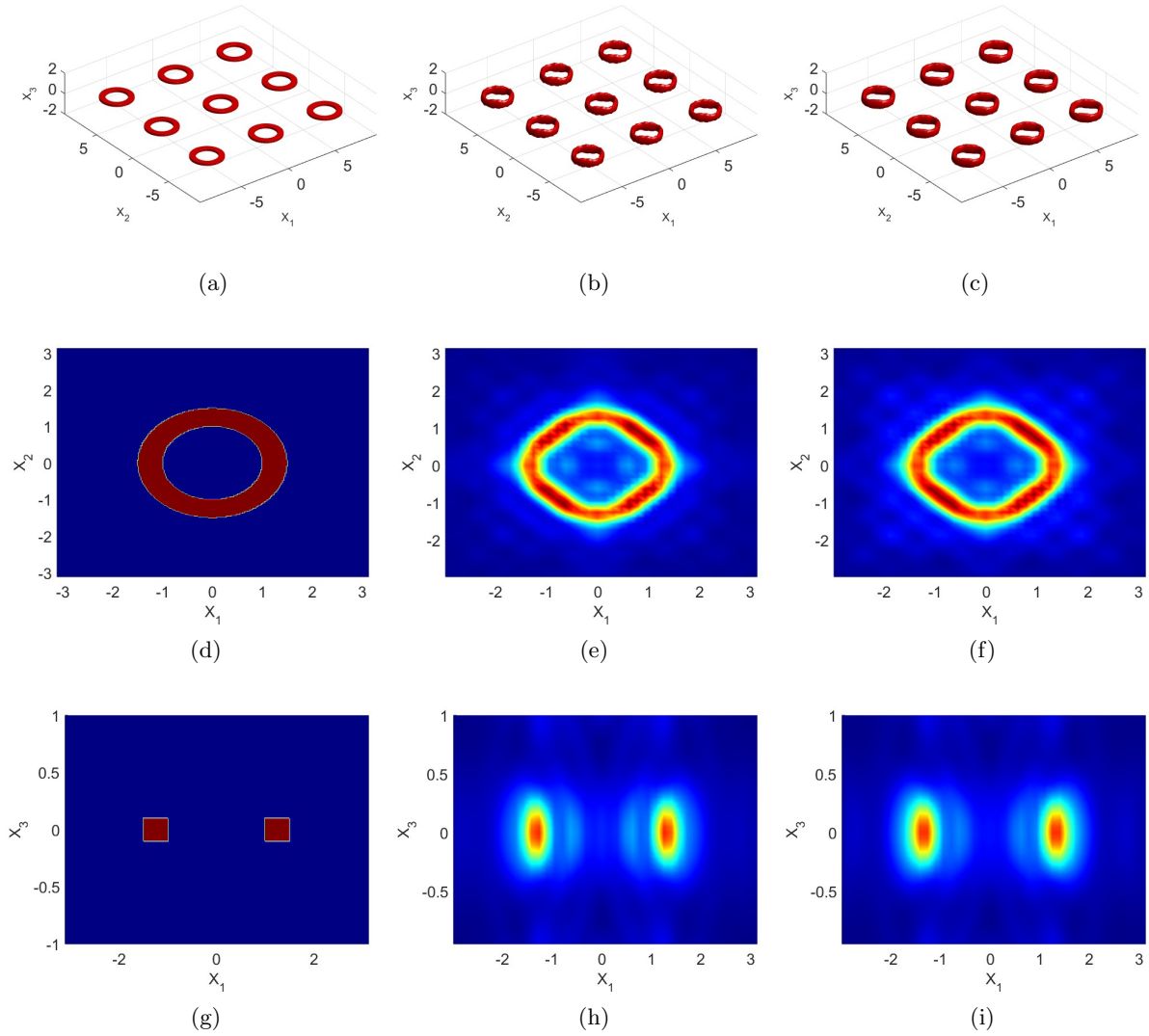

Figure 7: Reconstruction with different distances between the medium and the receivers. First column (a, d, g): True geometry in 3D and 2D views. Second column (b, e, h): reconstruction with $h = 1$. Third column (c, f, i): reconstruction with $h = 2.5$.

robustness against high levels of noise in the data.

The resolution analysis of the imaging functional relies on an integral representation and the Rayleigh expansion of quasi-periodic electromagnetic fields. The imaging functional is proved to be associated with an integral operator whose the kernel function has a strong peak when the sampling point lies within the unknown domain and has a much smaller value as the point moves away from this region. However, this analysis remains incomplete. We have also established the method's stability: as the noise level tends to zero, the difference between imaging functional values with and without noise converges to zero. Future research will focus on providing a complete theoretical justification for this method. Additionally, we aim to extend our investigation to elastic inverse

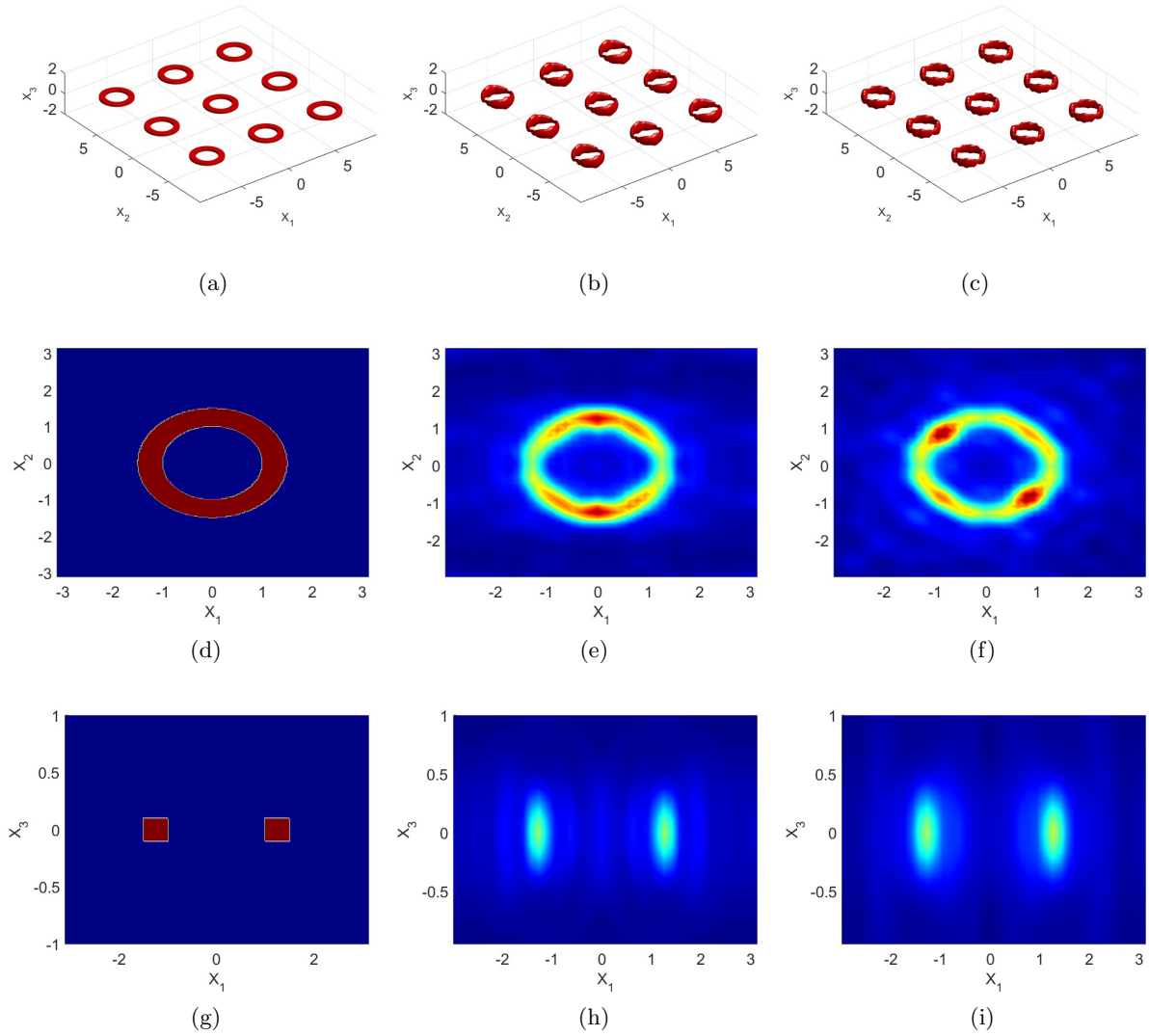

Figure 8: Reconstruction with different values of α_1 and α_2. First column (a, d, g): True geometry in 3D and 2D views. Second column (b, e, h): reconstruction with $\alpha_1 = 0$ and $\alpha_2 = \pi\sqrt{2}$. Third column (c, f, i): reconstruction with $\alpha_1 = \alpha_2 = \pi$.

scattering.

Numerically, our method demonstrates excellent performance across various periodic media and parameter sets. Specifically, it remains largely unaffected by the number of evanescent modes used, noise levels in the data, and distances between the medium and the receivers. As expected, the reconstruction stabilizes as the number of incident sources increases. Different values of α_1 and α_2 may slightly affect reconstructions. Furthermore, we conducted a comparative study with the factorization and orthogonality sampling methods. Notably, our method's regularization-free nature, relying solely on propagating modes, contributes to its superior stability compared to the factorization method. In all test cases, our reconstruction quality surpasses that of the orthogonality

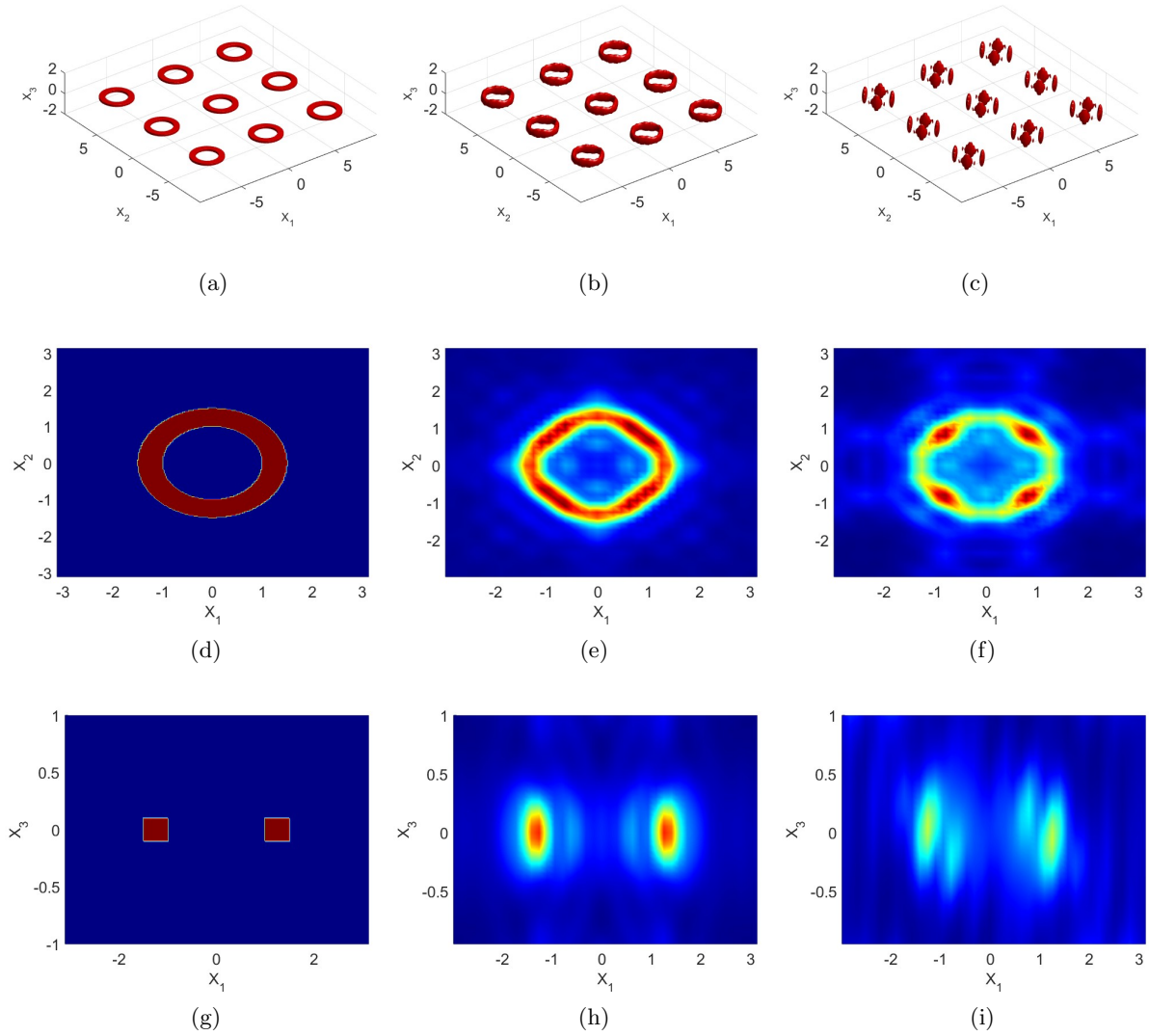

Figure 9: Comparison with the orthogonality sampling method for the ring. First column (a, d, g): True geometry in 3D and 2D views. Second column (b, e, h): reconstruction with the new sampling method. Third column (c, f, i): reconstruction with the orthogonality sampling method.

sampling method. This detailed numerical study of the method shows its great potential in solving the inverse problem of interest.

Acknowledgment. The work of the D.-L. Nguyen and T. Truong was partially supported by NSF Grant DMS-2208293.

References

[1] T. Arens and N. I. Grinberg. A complete factorization method for scattering by periodic structures. *Computing*, 75:111–132, 2005.

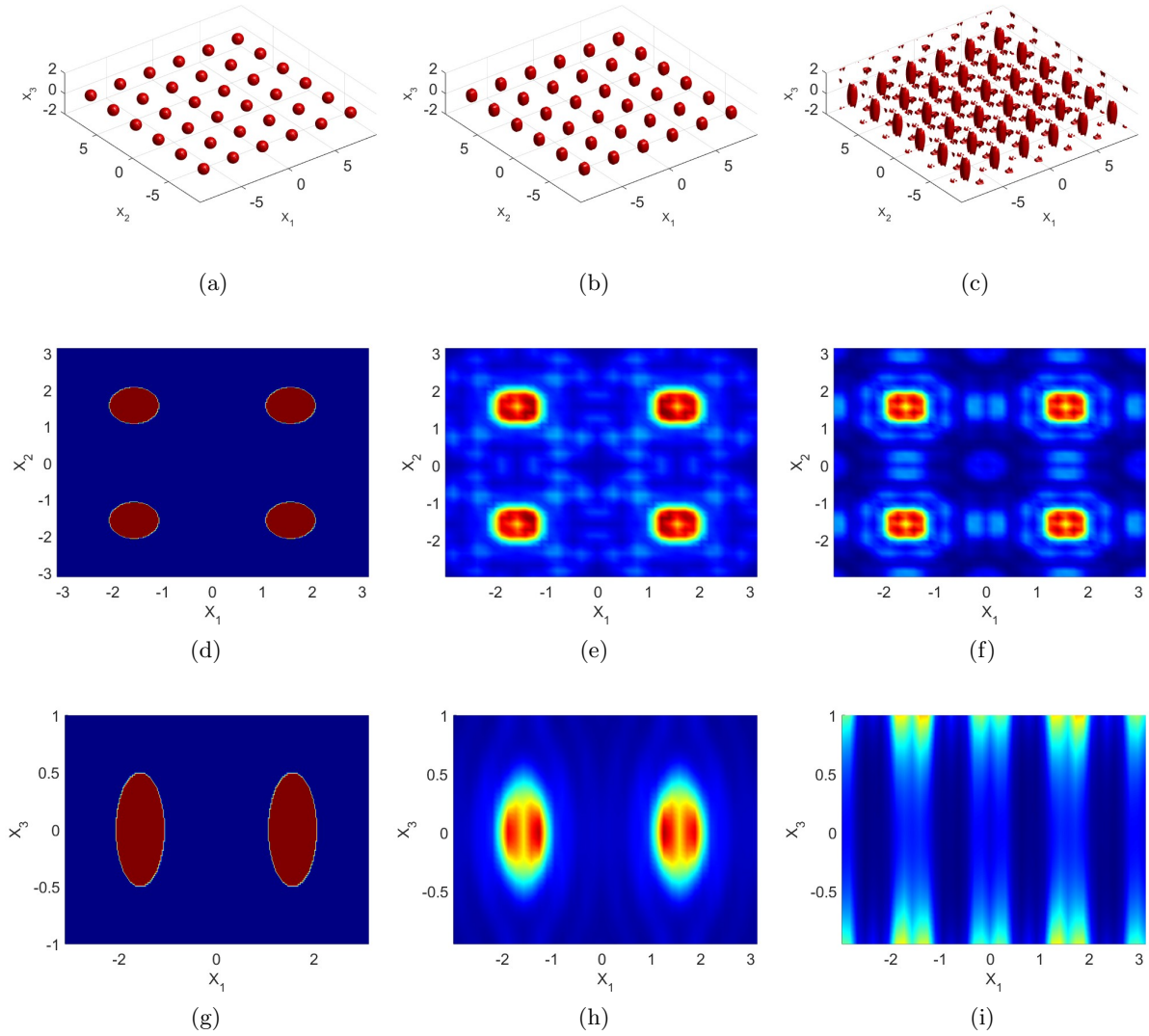

Figure 10: Comparison with the orthogonality sampling method for the sphere. First column (a, d, g): True geometry in 3D and 2D views. Second column (b, e, h): reconstruction with the new sampling method. Second column (c, f, i): reconstruction with the orthogonality sampling method.

[2] T. Arens and A. Kirsch. The factorization method in inverse scattering from periodic structures. *Inverse Problems*, 19:1195–1211, 2003.

[3] T. Arens. Scattering by biperiodic layered media: The integral equation approach. Habilitation Thesis, Universität Karlsruhe, 2010.

[4] G. Bao, T. Cui, and P. Li. Inverse diffraction grating of Maxwell's equations in biperiodic structures. *Optics Express*, 22:4799–4816, 2014.

[5] G. Bao and P. Li. *Maxwell's Equations in Periodic Structures*. Series on Applied Mathematical Sciences. Science Press, Beijing/Springer, Singapore, 2022.

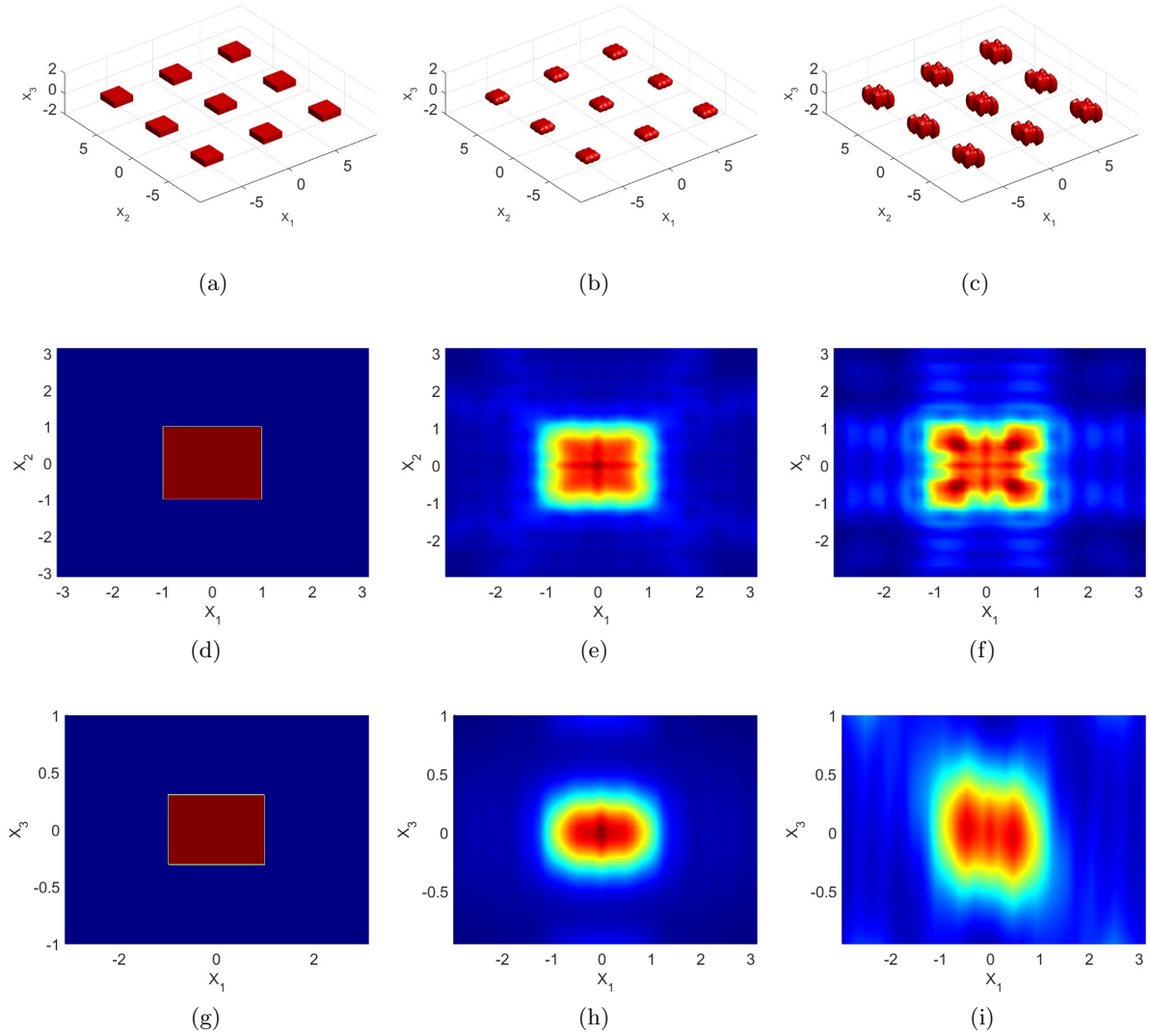

Figure 11: Comparison with the orthogonality sampling method for the cube. First column (a, d, g): True geometry in 3D and 2D views. Second column (b, e, h): reconstruction with the new sampling method. Second column (c, f, i): reconstruction with the orthogonality sampling method.

[6] Y. Boukari, H. Haddar, and N. Jenhani. Analysis of sampling methods for imaging a periodic layer and its defects. *Inverse Problems*, 39:055001, 2023.

[7] F. Cakoni, H. Haddar, and T.-P. Nguyen. New interior transmission problem applied to a single Floquet–Bloch mode imaging of local perturbations in periodic media. *Inverse Problems*, 35:015009, 2019.

[8] W. Dorfler, A. Lechleiter, M. Plum, G. Schneider, and C. Wieners. *Photonic Crystals: Mathematical Analysis and Numerical Approximation*. Springer, Basel., 2012.

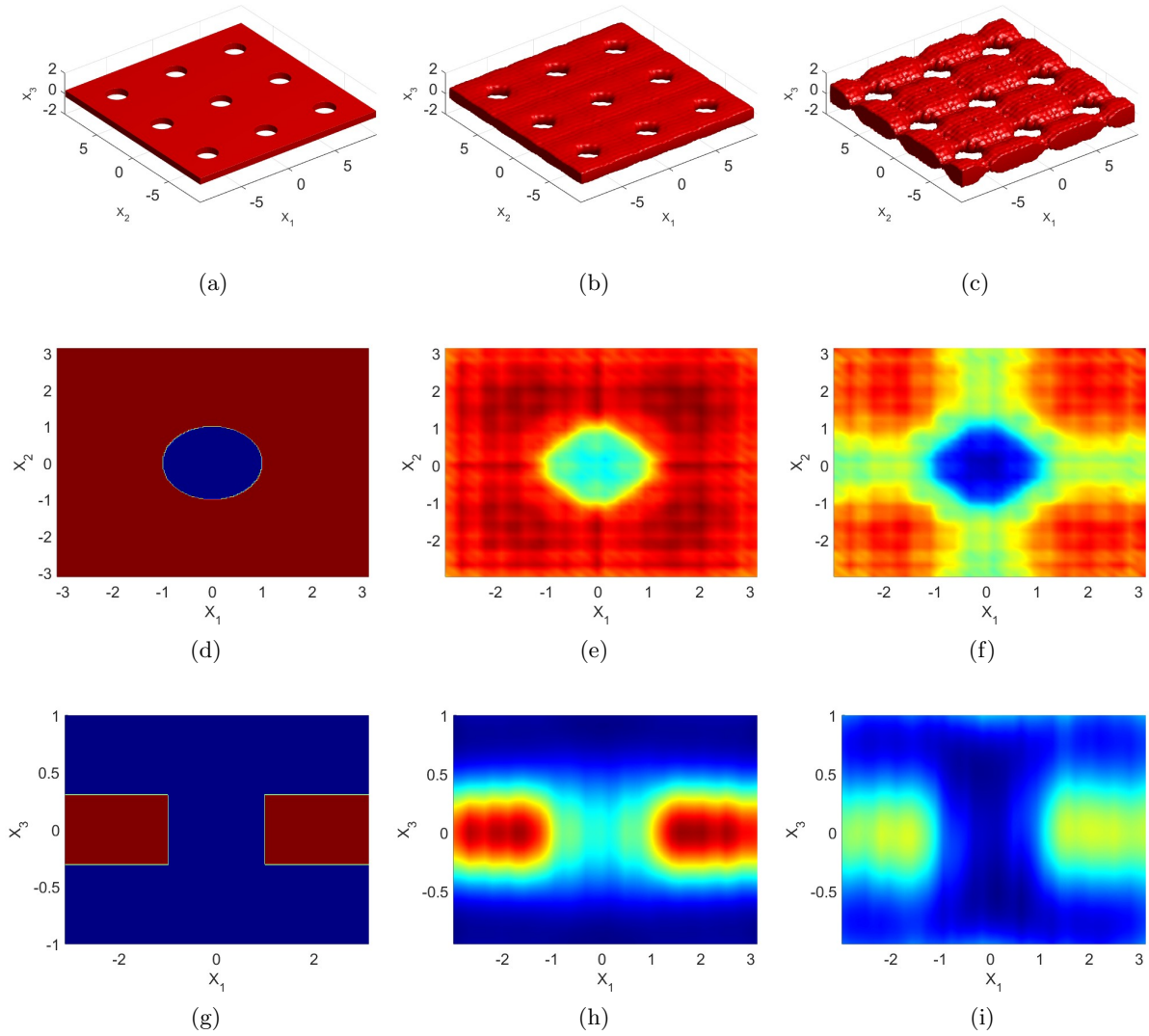

Figure 12: Comparison with the orthogonality sampling method for the perforated sheet. First column (a, d, g): True geometry in 3D and 2D views. Second column (b, e, h): reconstruction with the new sampling method. Second column (c, f, i): reconstruction with the orthogonality sampling method.

[9] J. Elschner, G. Hsiao, and A. Rathsfeld. Grating profile reconstruction based on finite elements and optimization techniques. *SIAM J. Appl. Math.*, 64:525–545, 2003.

[10] J. Elschner and G. Hu. An optimization method in inverse elastic scattering for one-dimensional grating profiles. *Commun. Comput. Phys.*, 12:1434–1460, 2012.

[11] R. Griesmaier. Multi-frequency orthogonality sampling for inverse obstacle scattering problems. *Inverse Problems*, 27:085005, 2011.

[12] H. Haddar and A. Konschin. Factorization method for imaging a local perturbation in inhomogeneous periodic layers from far field measurements. *Inverse Probl. Imaging*, 14:33–52, 2020.

[13] H. Haddar and T.-P. Nguyen. Sampling methods for reconstructing the geometry of a local perturbation in unknown periodic layers. *Comput. Math. Appl.*, 74:2831–2855, 2017.

[14] I. Harris and D.-L. Nguyen. Orthogonality sampling method for the electromagnetic inverse scattering problem. *SIAM J. Sci. Comput.*, 42:B72–B737, 2020.

[15] K. Ito, B. Jin, and J. Zou. A direct sampling method for inverse electromagnetic medium scattering. *Inverse Problems*, 29:095018, 2013.

[16] X. Jiang and P. Li. Inverse electromagnetic diffraction by biperiodic dielectric gratings. *Inverse Problems*, 33:085004, 2017.

[17] S. Kang, M. Lambert, and W.-K. Park. Direct sampling method for imaging small dielectric inhomogeneities: analysis and improvement. *Inverse Problems*, 34:095005, 2018.

[18] A. Lechleiter. Imaging of periodic dielectrics. *BIT*, 50:59–83, 2010.

[19] A. Lechleiter and D.-L. Nguyen. Factorization method for electromagnetic inverse scattering from biperiodic structures. *SIAM J. Imaging Sci.*, 6:1111–1139, 2013.

[20] A. Lechleiter and R. Zhang. Reconstruction of local perturbations in periodic surfaces. *Inverse Problems*, 34:035006, 2018.

[21] D.-L. Nguyen. A volume integral equation method for periodic scattering problems for anisotropic Maxwell's equations. *Appl. Numer. Math.*, 98:59–78, 2015.

[22] D.-L. Nguyen. The Factorization method for the Drude-Born-Fedorov model for periodic chiral structures. *Inverse Probl. Imaging*, 10:519–547, 2016.

[23] D.-L. Nguyen, K. Stahl, and T. Truong. A new sampling indicator function for stable imaging of periodic scattering media. *Inverse Problems*, 39:065013, 2023.

[24] T.-P. Nguyen. Differential imaging of local perturbations in anisotropic periodic media. *Inverse Problems*, 36:034004, 2020.

[25] R. Potthast. A study on orthogonality sampling. *Inverse Problems*, 26:074015, 2010.

[26] K. Sandfort. *The factorization method for inverse scattering from periodic inhomogeneous media*. PhD thesis, Karlsruher Institut für Technologie, 2010.

[27] J. Yang, B. Zhang, and R. Zhang. A sampling method for the inverse transmission problem for periodic media. *Inverse Problems*, 28:035004, 2012.

[28] R. Zhang and B. Zhang. Near-field imaging of periodic inhomogeneous media. *Inverse Problems*, 30:045004, 2014.

[29] J. Zheng, J. Cheng, P. Li, and S. Lu. Periodic surface identification with phase or phaseless near-field data. *Inverse Problems*, 33:115004, 2017.